

Modeling of Nonlinear Ultrashort Optical Pulse Propagation

by

Gregory Joseph Stein

B.S., Applied & Engineering Physics, Cornell University (2013)

Submitted to the Department of Electrical Engineering and
Computer Science

in partial fulfillment of the requirements for the degree of
Master of Science in Electrical Engineering and Computer Science
at the

MASSACHUSETTS INSTITUTE OF TECHNOLOGY

September 2015

© Massachusetts Institute of Technology 2015. All rights reserved.

Author
.....

Department of Electrical Engineering and Computer Science
August 18, 2015

Certified by
.....

Franz X. Kärtner
Adjunct Professor
Thesis Supervisor

Certified by
.....

Erich P. Ippen
Elihu Thomson Professor of Electrical Engineering Emeritus
Professor of Physics Emeritus
Thesis Supervisor

Accepted by
.....

Leslie A. Kolodziejski
Chair of the Committee of Graduate Students

Modeling of Nonlinear Ultrashort Optical Pulse Propagation

by

Gregory Joseph Stein

Submitted to the Department of Electrical Engineering and Computer Science
on August 18, 2015, in partial fulfillment of the
requirements for the degree of
Master of Science in Electrical Engineering and Computer Science

Abstract

I present a numerical package, written in MATLAB, which provides a simplified scripting interface for simulating a host of ultrashort pulse propagation phenomena. With the proliferation of ultrashort laser technologies, the demand for efficient and accurate simulations has grown significantly. Here I introduce a linear-operator-based formalism for nonlinear pulse propagation beyond the slowly-varying-envelope approximation, which includes phenomena such as nonlinear wave mixing, plasma blue-shifting, and high harmonic generation. I also demonstrate the capabilities of our versatile simulation package, which can handle optical pulse propagation through a host of geometries and guiding structures. Finally, the simulation package is used to investigate a number of effects, particularly that of modulational instability in Kagome-type hollow-core photonic crystal fibers.

Thesis Supervisor: Franz X. Kärtner
Title: Adjunct Professor

Thesis Supervisor: Erich P. Ippen
Title: Elihu Thomson Professor of Electrical Engineering Emeritus
Professor of Physics Emeritus

Acknowledgments

There are a host of people whose support I would like to acknowledge. First and foremost, I would like to thank my advisors Franz Kärtner and Erich Ippen who provided both the equipment and the guidance necessary for the completion of this thesis. In addition, the research scientists at MIT, Jeff Moses, Kyung-Han Hong, and Guillaume Laurent, collectively provided a source of constant guidance relating to the work contained within this thesis and in the laboratory. Third, I thank the graduate students and postdoctoral scholars in the Kärtner group at MIT, namely Peter Kroger, Chien-Jen Lai, Chun-Lin Louis Chang, Phillip Donald Keathley, Houkun Liang and Jonathas Siqueira. Their discussions, feedback and input were invaluable for determining how to make a simulation tool which was capable of supporting the variety of experiments undertaken in our laboratory. In addition, I gratefully acknowledge the hard work of graduate student Krishna Murari and research scientist Axel Ruehl, with whom I worked most closely to obtain the experimental data relating to the Kagome fibers.

I would also like to thank my friends and family for bearing with me during my time in graduate school thus far and through the thesis writing process. Most of all, I'd like to thank my fiancée Lucia Rafanelli, without whose steadfast support, I would not have made it this far.

Contents

1	Introduction	15
1.1	Kagome Hollow Core Photonic Crystal Fibers	16
1.2	Modulational Instability	18
1.3	Simulation Package	20
2	Ultrashort Pulse Propagation	23
2.1	Linear Propagation	26
2.1.1	Linear Propagation Operator	28
2.1.2	Spatial Integral Transformations	32
2.2	Field Conventions	36
2.3	Bound Nonlinear Optics	37
2.3.1	Self-Phase Modulation	38
2.3.2	Wave Mixing	40
2.4	Plasma and High Harmonic Generation	40
3	Numerical Package Architecture	45
3.1	Class Hierarchy	48
3.1.1	Data Manager [npDataManager]	48
3.1.2	Coordinate System [npCoord]	49
3.1.3	Field [npField]	51
3.1.4	Optical Material [npMat]	52

3.1.5	Optical Element [npEle]	52
3.2	Propagation Control Flow	53
3.2.1	Linear Propagation Step	54
3.2.2	Nonlinear Propagation Step	56
3.2.3	High Harmonic Generation Step	58
4	Simulation Experimental Results	61
4.1	Vacuum Linear Propagation	61
4.2	Nonlinear Self-Focusing	63
4.3	Degenerate Four Wave Mixing	65
4.4	Mid-Infrared Driven High Harmonic Generation	68
5	Pulse Compression in Kagome Fibers	73
5.1	Compression and Modulational Instability	74
5.2	Pulse Compression Results	80
5.2.1	Mid-Infrared Self-Compression	81
5.2.2	Picosecond Mid-Infrared Experiments	84
5.3	Pulse Compression Discussion	89
6	Conclusion & Future Work	93

List of Figures

1-1	A visual microscope image of the end-face of a 7-cell Kagome HC-PCF	18
1-2	A simulation of nonlinear pulse compression, subject to Eq. (1.3), in a $2 \mu\text{m}$ guiding Kagome Photonic Crystal Fiber. Notice that at the output (bottom plots), the transform limited (TL) pulse is much shorter than it is at the input, owing to a broadened spectrum. In addition, notice that, after self-phase modulation, the pulse and its spectrum are no longer Gaussian.	19
3-1	Schematic showing an example simulation, which corresponds to an experiment to study nonlinear optics in a Kagome hollow core photonic crystal fiber. In the setup, an optical waveform is focused into a gas-filled Kagome fiber, which, in the model, requires prop- agating the pulse through the focusing optic and vacuum before it reaches the fiber itself.	47
4-1	Example propagation of a Gaussian beam through vacuum, to demonstrate the basic capabilities of the simulation package. As ex- pected, the beam, which starts in a collimated state, has diffracted at the output and is both larger and has a non-flat phase profile. Notice that the beam matches the analytic solution extremely well, showing errors only on the order of 10^{-8} at the output.	63

5-1	Plots of the fundamental mode (FM) profiles for a 7-cell Kagome fiber and a Cylindrical Capillary of comparable radii, corresponding to a capillary core radius of $29 \mu\text{m}$. Also shown is the difference between the two profiles, which shows good agreement between the two profiles. Because of the $\pi/3$ rotational symmetry in the Kagome fiber, the profile is roughly hexagonal, while the capillary and its profile are both rotationally invariant.	76
5-2	Plot comparing the simulated gain versus the analytic model. Note how well the two profiles agree with one another. At low noise levels, the additional terms ignored by the analytic model make very little difference, however, as is discussed later on, this approximation eventually falls apart.	79
5-3	Simulations matching the parameters of Balciunas et al[4] showing the evolution of the temporal profile of the 80 fs pulse as it propagates through 20 cm of Xenon-filled Kagome fiber. During propagation, the pulse experiences self-compression, and produces a single soliton-like pulse at the output. The colorbar on the right displays the field intensity.	82
5-4	Individual temporal profiles corresponding to vertical cuts taken from Fig. 5-3. As the pulse propagates, a modulation forms and grows until, after the formation of an optical shock, a stable pulse forms at the output.	83

5-5 Evolution of a pulse as it passes through a Kagome fiber compressor as in Balciunas et al[4]. However, unlike the publication and the results shown in Fig. 5-3, the input pulse energy and duration are doubled (so as to keep the peak intensity fixed). This results in the formation of two peaks at the output, rather than a single soliton. This shows how the pulse compressor may be limited in the sorts of inputs it can handle.	84
5-6 Experimental retrieval of the output field (from a FROG) of our Kagome fiber pulse compressor for a $560 \mu\text{J}$ input energy. There is a clear, sharp temporal feature which is mostly compressed which contains just under 40% of the pulse energy.	85
5-7 Simulated Kagome fiber compression results (temporal profiles and spectra) illustrating the effects of adding an aperiodic modulation to the pulse. Three different pulses are propagated through a 4 meter Kagome fiber: one without a pedestal, one with a narrow-band pedestal, and one with a wide-band pedestal. As the bandwidth of the pedestal is increased, the output profile is increasingly distorted, which can result in sharp intensity peaks.	87
5-8 Intensity profile evolution as a function of propagation distance for a narrow-band modulation. Even though the bandwidth of the pedestal at the input is relatively narrow, the profile still splits into isolated peaks by the output. After the peaks form, they do not behave as solitons and continue to change in the presence of dispersion. The <i>forking</i> behavior, in which each peak splits into separate peaks after further propagation, is typical for an overly-dispersion-compensated pulse-compressor.	88

List of Tables

Chapter 1

Introduction

As nonlinear optics has matured since its inception over half a century ago[3], it has been largely driven by the demand for increasingly powerful and versatile light sources. Nonlinear frequency generation facilitates this process, during which optical energy centered about one wavelength is transferred to another[5]. Historically, approaches to frequency conversion have been dominated by predominantly free-space techniques[6, 22], but the regions of nonlinear interaction are limited in many cases by the diffraction length of the pulses, thereby placing a fundamental restriction on the overall conversion efficiency.

More recently, there has been an emphasis on propagation geometries which can be used to confine ultrashort pulses for longer interaction regions in order to overcome this difficulty. Cylindrical hollow capillaries are one such structure[23], however, they are limited by relatively strong coupling between modes in the presence of nonlinearities and suffer from high losses over lengthy propagation distances. Though the fundamentally multi-mode cylindrical capillaries have shown promise for weak guidance, hollow core photonic crystal fibers (HC-PCF) have demonstrated low-loss, single-mode guidance of high energy optical pulses for extended distances[19, 10]. In addition, these fibers can be filled with gases

and can support a variety of nonlinear optical interactions including self-phase modulation[33], third-harmonic generation[26] and even extreme nonlinear phenomena like high-harmonic generation[16, 29].

Finally, for applications which reach peak intensities high enough to generate appreciable plasma densities[8] inside of a gas filled hollow core fiber, it is not straightforwardly understood that having a guiding structure even provides an advantage over a free-space geometry, as in the case of high harmonic generation[18]. As such, the tools used to simulate nonlinear ultrashort pulse propagation must be sufficiently flexible so as to confirm that the structure does indeed enhance the targeted result. This is only possible if the model is capable of easily switching between different confining geometries and free space. My simulation package, which I introduce in a later section, is designed with these constraints in mind.

1.1 Kagome Hollow Core Photonic Crystal Fibers

For many nonlinear optics applications, particularly for nonlinear pulse compression, using a free space geometry is unsuitable and confining geometries are necessary to enhance the effect of the nonlinearity. For pulses at relatively low peak intensities, silica fibers can be used. In addition, the mode area of the fiber can be customized to allow the propagation of only a single mode, which can help to clean the spatial beam profile at the output. However, at high pulse energies, silica fibers immediately succumb to damage and cannot be used.

Hollow cylindrical capillaries can be used to confine pulses at very high intensities. The idea, first proposed by Marcatili[23], is that the large jump in refractive index between the gas-filled core of the structure and the glass outer layer, which has an index $n \approx 1.5$, confines the field to the core. Only a negligible amount of the field exists outside of the core and the capillary modes can be approximated as those of a cylindrical metallic waveguide. It is well known that these modes

are given in terms of zeroth order Bessel functions such that mode m is

$$M_m(r) = J_0 \left(r \frac{u_{0m}}{a} \right) \quad (1.1)$$

where a is the radius of the fiber and u_{0m} is the m th zero of the Bessel function $J_0(x)$, so that the field is identically zero at the boundary of the fiber. However, because the waveguide is not perfectly metallic and there is some field in the glass, each mode m is lossy with a loss coefficient, $\alpha_m = \Im[\beta_m]$ approximately equivalent to[9]

$$\alpha_m = \frac{1}{a^3} \left[\frac{u_{0m}c}{\omega n(\omega)} \right]^2 \frac{n_c^2(\omega) + 1}{\sqrt{n_c^2(\omega) - 1}} \quad (1.2)$$

where ω is the radius of the hollow fiber core, ω is the angular frequency of laser, c is the speed of light, $n(\omega)$ is the frequency dependent index of the core and $n_c(\omega)$ is the index of the glass cladding. In particular, note that the fundamental mode, the lowest order solution, has a non-trivial loss coefficient. Additionally, the enhancement of nonlinearities during propagation is often aided by higher peak intensities, which can be achieved with a smaller core diameter. Since the loss scales with the cube of the radius of the pulse, so that thinner capillaries experience dramatically higher loss for all modes, using this geometry is far from ideal in circumstances when tighter confinement is an asset.

Because of the fundamentally multi-mode nature of the hollow cylindrical capillary and the high loss associated with the fundamental mode, it is said to be *weakly guiding*. By contrast, the Kagome type Hollow Core Photonic Crystal fiber displays strong guidance of the pulse. The unique structure of the fiber, shown in Figure 1-1, is capable of localizing the pulse to the very center of the hollow core. In addition, the Kagome fiber can be considered a single mode geometry, so that any energy transferred into any of the higher order modes, the modes which are not the fundamental, is almost immediately lost. This prevents coherent transfer

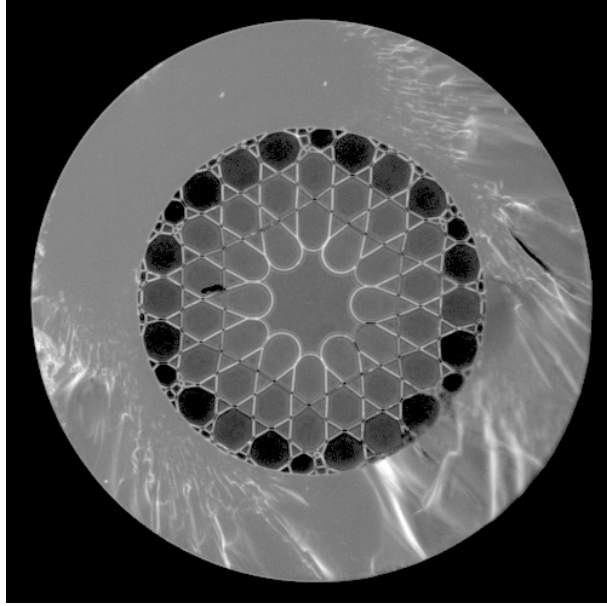


Figure 1-1: A visual microscope image of the end-face of a 7-cell Kagome HC-PCF

of energy away from the fundamental mode and reduces the overall loss. Furthermore, one of the most incredible properties of the Kagome fiber is its extremely low loss, allowing propagation of tightly confined pulses over kilometer-order distances. Finally, even though the fiber is microstructured, the intensity at the glass lattice is only roughly 10^{-4} of the peak intensity, which means that, if the input coupling is high, the fiber is very resistant to damage when compared to solid-core fibers.

1.2 Modulational Instability

The properties of the Kagome fiber, including tight-single-mode guidance, low loss and high damage threshold, make it an ideal tool for nonlinear optics. In particular, though they have proven useful for a host of applications, as specified in the introduction, this thesis aims to study phenomena related to nonlinear pulse compression. In a nonlinear pulse compressor, self-phase modulation from

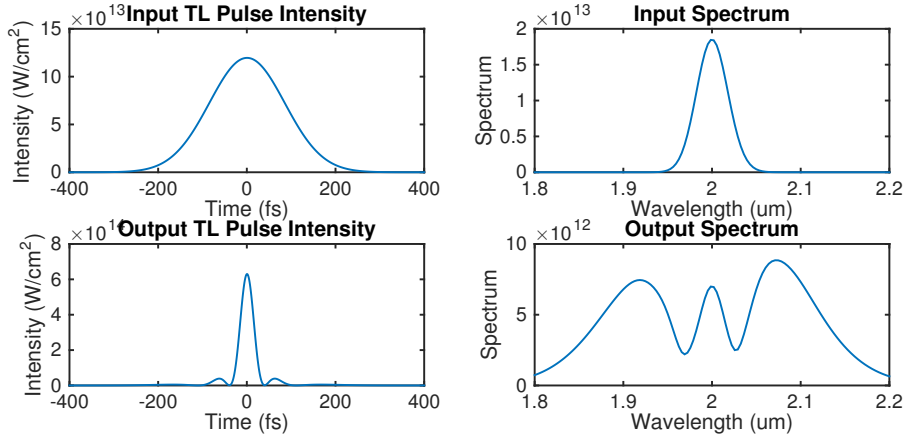


Figure 1-2: A simulation of nonlinear pulse compression, subject to Eq. (1.3), in a $2 \mu\text{m}$ guiding Kagome Photonic Crystal Fiber. Notice that at the output (bottom plots), the transform limited (TL) pulse is much shorter than it is at the input, owing to a broadened spectrum. In addition, notice that, after self-phase modulation, the pulse and its spectrum are no longer Gaussian.

a nonlinear medium is used to broaden the spectrum of the pulse, as in Fig. 1-2. Because of the conjugate relationship between the transform limited duration a pulse and its spectral width, this process allows for a pulse to be shortened, or compressed, beyond its input duration.

This effect has been experimentally verified, for sub-picosecond pulses, and has been able to achieve relatively high compression factors, the ratio of the input pulse duration to that of the output. Most astonishing, however, is the high energy throughput at the output of the system, which can be greater than 90%. By contrast, nonlinear pulse compressors are otherwise constructed with cylindrical capillaries, which, for similar input parameters, typically have peak efficiencies of 50%-60%.

Despite the usefulness of spectral broadening, experiments to compress 3.4 picosecond pulses in the Kärtner group have been met with resistance in the form of damage in our Kagome fiber after propagation and poor temporal beam profiles. It was quickly discovered that this behavior was likely the result of amplification

of noise in our system, which limits the amount of spectral broadening that can be achieved in a compressor.

The equation for pulse propagation in the presence of self-phase modulation is[1]

$$i \frac{\partial E}{\partial z} = \frac{\beta_2}{2} \frac{\partial^2 E}{\partial t^2} - \gamma |E|^2 E , \quad (1.3)$$

where E is the electric field amplitude, β_2 is the 2nd order dispersion, and γ is the nonlinear parameter (which will be defined in a later chapter). In the presence of a small perturbation e to the electric field, the propagation equation can be reduced to

$$i \frac{\partial e}{\partial z} = \frac{\beta_2}{2} \frac{\partial^2 e}{\partial t^2} - \gamma E_0^2 (e + e^*) . \quad (1.4)$$

It can be shown that, in the presence of anomalous dispersion and a continuous-wave beam input, the noise will experience exponential gain, a phenomena known as modulational instability (MI). This is often the limiting factor in compression experiments for the Kagome fiber.

In this thesis, I study this effect. In particular, I will study how the rates of modulational instability and spectral broadening compare to one another, and how that information can be used to maximize the potential of a pulse compressor in the face of exponentially growing noise. I aim to understand how tuning the parameters of the input can help to maximize the compression factor and maintain a clean temporal beam profile at the output.

1.3 Simulation Package

In an effort to satisfy the demand for increasingly tunable and high yield laser sources, the sophistication of nonlinear optics experiments has grown significantly over the last decade. Particularly, there has been an emphasis on the geometries in which the conversion occurs, notably hollow-core photonic crystal fibers, which

are capable of guiding high-peak-power pulses[19, 10]. As a consequence of the variety of techniques used for nonlinear optics experiments, there are still many open questions concerning the relative efficacy of different approaches.

The necessity for theoretical support is thus obvious, since numerical models are capable of providing detailed information that is often inaccessible in experiments, especially those involving very strong nonlinearities, and can be done more quickly and inexpensively. However, comparing the relative merits of different experimental approaches has become increasingly difficult, and efforts to understand the underlying behavior of the electric fields during propagation has resulted in the development of simulations which are often as specific in scope as the experiments they are designed to reproduce.

To address this ubiquitous complication, I present a code which is designed with a higher level of abstraction than the typical optical pulse propagation simulation described above. It aims to provide a simple scripting interface for creating easily modified and reusable code. This thesis is devoted to a description of the framework underlying this simulation package, along with a set of benchmark test uses, and, subsequently, a more in-depth analysis of a number of nonlinear phenomena, including modulational instability in photonic crystal fibers.

My simulation package follows a class-based architecture, which allows for the code to be easily modified with the creation of user-defined sub-classes. This is critical for the long-term re-usability of the package; users can easily create modules devoted to the study of new phenomena and share them with colleagues and collaborators. With this in mind, the purpose of this thesis is not to introduce a “completed” numerical package. On the contrary, there are still a handful of commonly studied nonlinear effects which have yet to be implemented. However, I do present a framework which is designed to be easily extended to support arbitrary nonlinearities which may appear in paraxial pulse propagation. This

work will describe how the code operates in sufficient detail so that it may serve as a tutorial for extending the functionality of the model.

In this thesis, I will describe the structure of the simulation code I have created to address the aforementioned difficulties facing the nonlinear optics community, particularly nonlinearities in photonic crystal fibers. The code follows an object-oriented paradigm and is programmed entirely in MATLAB, which was chosen for its ubiquity, ease of use, and powerful CPU/GPU parallelization features for matrix-oriented numerical applications.

Thorough simulation efforts have been made recently by Tani et al[32] to characterize the behavior of ultrashort pulses in the presence of different nonlinearities that these unique fibers are capable of supporting. However, as there are still a number of open questions regarding the exact nature of the low-loss guidance in Kagome HC-PCF, having a simulation code which is capable of keeping pace with the ever-changing nature of our understanding is critical for quickly advancing this expanding area.

Chapter 2

Ultrashort Pulse Propagation

In addition to flexibility, a general-purpose numerical code must be accurate for a wide variety of initial conditions and experimental configurations. Many codes for ultrashort pulse propagation are built upon the sorts of equations typically found in textbooks for nonlinear optics. However, these equations are often geared towards analytic analysis, and are derived with approximations, notably the pervasive slowly-varying envelope approximation, which allow the equations to be more easily analyzed or solved analytically. Under the slowly-varying envelope approximation, the time derivative terms present in the wave equation are expanded into a Taylor series about the central frequency of the pulse[5]. Higher order derivatives are often dropped, owing to their often small contributions to pulse propagation. While this is sufficient for some applications, as the laser community pushes further and further into the realm of pulses with features on the order of a single optical cycle, these equations are not entirely accurate and, to satisfy energy conservation, must me modified at what can be a considerable effort.

There have been successful efforts[28, 5, 25] to include and understand these additional derivative terms in the equations for ultrashort pulse propagation in the

presence of wave-mixing nonlinearities, in effect moving beyond the slowly-varying limit. However, though the coupled equations which result are more accurate than their approximated counterparts, the equations are more tedious to derive and are often far more complicated to understand and to translate into a numerical model. In the context of simulations, making these sorts of series expansions is wasteful. Because the frequency content of the pulses can be directly obtained from the Fourier transform of the fields, it is possible to derive a set of coupled equations which accurately simulate the nonlinear propagation of an ultrashort pulse without any prior knowledge of the initial properties of the fields. Here these equations are derived for a variety of nonlinearities and show that, in addition to their accuracy, their lack of a large number of partial derivatives greatly simplifies their incorporation into the numerical model.

The derivation begins with Maxwell's Equations[20]:

$$\nabla \cdot \mathbf{D} = \rho , \quad (2.1a)$$

$$\nabla \cdot \mathbf{B} = 0 , \quad (2.1b)$$

$$\nabla \times \mathbf{H} = \mathbf{J} + \frac{\partial \mathbf{D}}{\partial t} , \quad (2.1c)$$

$$\nabla \times \mathbf{E} = -\frac{\partial \mathbf{B}}{\partial t} . \quad (2.1d)$$

where the field quantities, \mathbf{E} , \mathbf{B} , \mathbf{D} , and \mathbf{H} are all complex valued vector functions of space and time.

For optical pulses it may be assumed that the propagation materials have no free charges, which means that both the charge ρ and current density \mathbf{J} are identically zero. In addition, optical materials are typically non-magnetic, so that

the constitutive relations which relate the field quantities are

$$\mathbf{B} = \mu_0 \mathbf{H} , \quad (2.2a)$$

$$\mathbf{D} = \epsilon_0 \mathbf{E} + \mathbf{P} . \quad (2.2b)$$

where \mathbf{P} is the material polarization.

Under these conditions, Maxwell's Equations can be combined to obtain

$$\nabla \times \nabla \times \mathbf{E} + \mu_0 \frac{\partial^2 \mathbf{D}}{\partial t^2} = 0 . \quad (2.3)$$

To further reduce this, it is useful to introduce the well-known vector identity

$$\nabla \times \nabla \times \mathbf{E} = \nabla(\nabla \cdot \mathbf{E}) - \nabla^2 \mathbf{E} , \quad (2.4)$$

where ∇^2 is the Laplacian operator. In addition, the common assertion that $\nabla \cdot \mathbf{E}$ is negligibly small[5] is employed, so that Eq. (2.3) becomes

$$\frac{\partial^2 \mathbf{E}}{\partial z^2} + \nabla_{\perp}^2 \mathbf{E} - \frac{1}{c^2} \frac{\partial \mathbf{E}}{\partial t^2} = \frac{1}{\epsilon_0 c^2} \frac{\partial^2 \mathbf{P}}{\partial t^2} , \quad (2.5)$$

where $c = (\epsilon_0 \mu_0)^{-1/2}$ is the speed of light. Finally, the form of the solution is known to be a propagating wave in the $+z$ direction, which is why the Laplacian operator has been broken into a second partial derivative with respect to z and the transverse Laplacian ∇_{\perp}^2 . This is the most general form of the wave equation, which governs electromagnetic pulse propagation.

2.1 Linear Propagation

For an isotropic, linear material, the material polarization \mathbf{P} responds linearly to the electric field so that

$$\mathbf{P} = \mathbf{P}_L = \epsilon_0 \hat{\chi}^{(1)}(\omega) \mathbf{E} , \quad (2.6)$$

in which $\hat{\chi}^{(1)}(\omega)$ is the linear electric susceptibility and \mathbf{P}_L is the linear contribution of the polarization. Notice that, because it is a function of the frequency ω , it behaves as an operator¹ in the time domain and is composed of a convergent power series of time derivatives. Working with such frequency dependent terms is discussed at length in the next section. Including this substitution means that the generalized wave equation from Eq. (2.5) becomes

$$\frac{\partial^2 \mathbf{E}}{\partial z^2} + \nabla_{\perp}^2 \mathbf{E} - \frac{\hat{n}^2}{c^2} \frac{\partial \mathbf{E}}{\partial t^2} = 0 , \quad (2.7)$$

where $\hat{n} = \sqrt{1 + \hat{\chi}^{(1)}}$ is the refractive index, which, like the linear susceptibility, also acts as a differential operator in the time domain.

For electromagnetic wave propagation, the simplest solution to Eq. (2.7) is a monochromatic plane wave of the form

$$\mathbf{E}(\mathbf{x}, t, z) = E_0 \hat{x} \exp [+i n(\omega_0) k_0(\omega_0) z - i \omega_0 t] , \quad (2.8)$$

where $k_0(\omega) = \omega/c$ is the free-space wavector and ω_0 is the angular frequency of the wave.

More generally, many plane waves of different frequencies can be summed to generate an electromagnetic pulse, which will travel along the $+z$ axis at its group velocity v_g , which is related to the refractive index. However, it is useful to operate in a reference frame which travels at the speed of the pulse so that its evolution

¹Operators are denoted by a hat symbol and are elements defined as a linear combination of partial derivatives.

may be studied. This can be done with the following substitution,

$$\mathbf{E}(\mathbf{x}, t, z) \Rightarrow \exp \left[i \frac{c}{v_g} \hat{k}_0 z \right] \mathbf{E}(\mathbf{x}, t, z) , \quad (2.9)$$

so that \mathbf{E} is now the electric field of the pulse in the traveling frame.

Not only is working in a moving reference frame useful for practical understanding, but it is essential for numerical modeling, in which the size of the windowed frame is finite, and far smaller than the total propagation distance. Notice that, like the refractive index, the phase term included here is also frequency dependent, since each of the plane wave terms, from which the pulse is constructed, will accumulate different amounts of phase depending on their central frequency as the frame is moved by a distance z . If one wished to directly apply the exponential shown in Eq. (2.9) in the time-domain, a Taylor series expansion would be necessary:

$$\exp \left[i n_g \hat{k}_0(\omega) z \right] = 1 + i n_g \hat{k}_0 z + \frac{1}{2} \left[i n_g \hat{k}_0 z \right]^2 + \mathcal{O} \left[\hat{k}_0^3 z^3 \right] . \quad (2.10)$$

Combining the wave equation in Eq. (2.7) with the substitution from Eq. (2.9) results in

$$\frac{\partial^2 \mathbf{E}}{\partial z^2} + 2 i n_g \hat{k}_0 \frac{\partial \mathbf{E}}{\partial z} = n_g^2 \hat{k}_0^2 \mathbf{E} - \nabla_{\perp}^2 \mathbf{E} + \frac{\hat{n}^2}{c^2} \frac{\partial^2 \mathbf{E}}{\partial t^2} , \quad (2.11)$$

which describes the evolution of a electromagnetic pulse in a reference frame moving with velocity $v_g = c/n_g$.

It is also important to make an approximation² in which the contribution from

²This is one of two different effects known as the *slowly varying envelope approximation*. The first (made here) in which the second derivative of \mathbf{A} with respect to z is dropped, is extremely important for solving boundary value differential equations, and is necessary for solution. The other, which is intentionally not made here, neglects the contributions from time derivative terms which arise in the presence of non-monochromatic waves. The second form of the slowly varying envelope approximation is far more inaccurate than the first, and in particular suffers from inaccuracy when working with multi-color or spectrally broad pulses. As such, great care is (rather uniquely) taken in this work to avoid making this approximation.

the second derivative in z of the field envelope $\mathbf{A}(\mathbf{x}, t, z)$ is neglected. This term is related to the electric field by

$$\mathbf{A}(\mathbf{x}, t, z) = \exp \left[i(\hat{n} - n_g)\hat{k}_0 z \right] \mathbf{E}(\mathbf{x}, t, z) \quad (2.12)$$

This is a common approximation in optical pulse propagation[1, 5]. It allows for a convenient simplification of the the second derivative of the field \mathbf{E} with respect to z so that:

$$\frac{\partial^2 \mathbf{E}}{\partial z^2} \approx 2i(\hat{n} - n_g)\hat{k}_0 \frac{\partial \mathbf{E}}{\partial z} + (\hat{n} - n_g)^2 \hat{k}_0^2 \mathbf{E} \quad (2.13)$$

This can be easily shown by plugging in the relation from Eq. (2.12) into the wave equation, dropping the second derivative of \mathbf{A} in z , and then inverting Eq. (2.12).

By introducing this modification into Eq. (2.11), and recognizing that

$$\hat{k}_0^2 = -\frac{1}{c^2} \frac{\partial^2}{\partial t^2} \quad (2.14)$$

the wave equation becomes, finally,

$$2i\hat{n}\hat{k}_0 \frac{\partial \mathbf{E}}{\partial z} = -\nabla_{\perp}^2 \mathbf{E} - 2\hat{n}(\hat{n} - n_g)\hat{k}_0^2 \mathbf{E} . \quad (2.15)$$

This is the form of the linear stationary wave equation which will be used for the remainder of this work.

2.1.1 Linear Propagation Operator

Solving Eq. (2.15) requires treating it as a boundary value problem, in which an input field is given at $z = 0$, $\mathbf{E}(\mathbf{x}, t, z = 0)$, and the field at an arbitrary output position $z = z_f$ is desired. Eq. (2.15) is a linear partial differential equation and, as such, in solving the differential equation as a function of z , the differential

operators on the right-hand-side, the transverse Laplacian and \hat{k}_0 , may be treated as scalars, effectively turning the problem into a first-order ordinary differential equation in z . This has a straightforward solution involving exponential functions. In this case, the solution is found to be given by:

$$\begin{aligned}\mathbf{E}(\mathbf{x}, t, z_f) &= \exp \left[i \frac{\nabla_{\perp}^2}{2\hat{n}\hat{k}_0} z_f + i\hat{k}_0 (\hat{n} - n_g) z_f \right] \mathbf{E}(\mathbf{x}, t, z = 0) \\ &= \hat{\mathcal{P}}(z_f) \mathbf{E}(\mathbf{x}, t, z = 0) .\end{aligned}\quad (2.16)$$

This solution can be easily verified by plugging Eq. (2.16) into the wave equation, Eq. (2.15), and recognizing that all of the differential operators commute with one another. The exponential operator acting on our input field in the second line of Eq. (2.16) is known as the propagation operator $\hat{\mathcal{P}}(z_f)$, named as such because it effectively propagates our field from $z = 0$ to $z = z_f$. Since it is an exponential function of operators, the straightforward way to solve this equation may be to expand the exponential into a Taylor series, as in (2.10), and calculate each term in the resulting expansion. However, integral transformations can alternately be used to accurately obtain the solution much more efficiently.

To demonstrate this idea, the effect the Fourier Transform has on a derivative in time applied to a function $A(t)$ can be observed. The Fourier Transform operator $\hat{\mathcal{F}}_{\omega}$ and its inverse $\hat{\mathcal{F}}_t$ are defined as follows

$$\begin{aligned}\hat{\mathcal{F}}_{\omega} &= \int_{-\infty}^{\infty} dt e^{-i\omega t} \\ \hat{\mathcal{F}}_t^{-1} &= \frac{1}{2\pi} \int_{-\infty}^{\infty} d\omega e^{+i\omega t}\end{aligned}\quad (2.17)$$

where, for clarity, the subscript of each operator shows the function variable of the output of the transformation. Given these definitions, it is well known that the

basis functions of the Fourier transform operator, complex exponential functions $e^{-i\omega t}$, are eigenvalues of the time derivative operator, which means that it is easy to show that, for some well-behaved function of time $A(t)$,

$$\hat{\mathcal{F}}_\omega \left[\frac{\partial}{\partial t} A(t) \right] = i\omega \hat{\mathcal{F}}_\omega [A(t)] , \quad (2.18)$$

This suggests that, if the Fourier transform can be easily evaluated, then applying any differential operator in time is as simple as multiplication in frequency space. As such, the Fourier transform can be employed to simplify the calculation of sophisticated differential operators. For example, recognizing that $\hat{\mathcal{F}}_\omega [\hat{k}_0] = k_0(\omega)$, since k_0 is defined in frequency space, it can be easily shown, using the Taylor expansion technique from Eq. (2.10) that

$$e^{i\hat{k}_0 z} \mathbf{E} = \hat{\mathcal{F}}_t^{-1} \left[\hat{\mathcal{F}}_\omega \left[e^{i\hat{k}_0 z} \mathbf{E} \right] \right] = \hat{\mathcal{F}}_t^{-1} \left[e^{i\hat{\mathcal{F}}_\omega [\hat{k}_0] z} \hat{\mathcal{F}}_\omega [\mathbf{E}] \right] = \hat{\mathcal{F}}_t^{-1} \left[e^{ik_0(\omega) z} \hat{\mathcal{F}}_\omega [\mathbf{E}] \right] . \quad (2.19)$$

This shows that applying the exponential operator to the field \mathbf{E} can be done very simply using the Fourier transform and its inverse. In fact, this is true in general for any linear operator so that, given the proper integral transformation in both space and time, the propagation operator $\hat{\mathcal{P}}(z_f)$ from Eq. (2.16) can be applied to the input field very easily.

As in the case of the Fourier transform, an integral transformation is sought whose basis functions are eigenfunctions of the transverse Laplacian operator ∇_\perp . It is described in the next section that the eigenfunctions and their eigenvalues will depend on the geometry of the problem, since they depend on boundary conditions and symmetries. In general, however, the spatial transformation (and inverse) are referred to as $\hat{\mathcal{S}}_{\mathbf{q}}$ (and $\hat{\mathcal{S}}_{\mathbf{x}}^{-1}$), which transforms a function of the transverse position \mathbf{x} and transforms it to a function of the reciprocal space vector \mathbf{q} (and back). In this case, we define $-\kappa^2(\mathbf{q})$, a scalar function of \mathbf{q} , to be the eigenvalue of the

transverse Laplacian operator,

$$\hat{\mathcal{S}}_{\mathbf{q}} [\nabla_{\perp}^2 \mathbf{E}] = -\kappa^2(\mathbf{q}) \hat{\mathcal{S}}_{\mathbf{q}} [\mathbf{E}] \quad (2.20)$$

so as to mirror the analogous property of the Fourier transform illustrated in Eq. (2.18).

Having defined integral transformations in both space $\hat{\mathcal{S}}_{\mathbf{q}}$ and time $\hat{\mathcal{F}}_{\omega}$, the complete transformation operator $\hat{\mathcal{C}}_{\mathbf{q}\omega}$ and its inverse $\hat{\mathcal{C}}_{\mathbf{x}t}^{-1}$ can be defined as compositions of the individual transformations:

$$\begin{aligned} \hat{\mathcal{C}}_{\mathbf{q}\omega} &= \hat{\mathcal{S}}_{\mathbf{q}} \circ \hat{\mathcal{F}}_{\omega} \\ \hat{\mathcal{C}}_{\mathbf{x}t}^{-1} &= \hat{\mathcal{F}}_t^{-1} \circ \hat{\mathcal{S}}_{\mathbf{x}}^{-1} \end{aligned} \quad (2.21)$$

With the introduction of these definitions, the solution to the propagation equation, Eq. (2.16), may now be rewritten in the following way:

$$\mathbf{E}(\mathbf{x}, t, z_f) = \hat{\mathcal{C}}_{\mathbf{x}t}^{-1} \left[\mathcal{P}(\mathbf{q}, \omega | z_f) \hat{\mathcal{C}}_{\mathbf{q}\omega} [\mathbf{E}(\mathbf{x}, t, z=0)] \right] \quad (2.22)$$

where the spectral propagation operator $\mathcal{P}(\mathbf{q}, \omega | z_f)$, a continuous function of \mathbf{q} and ω given z_f , transformed from Eq. (2.16), is defined as

$$\mathcal{P}(\mathbf{q}, \omega | z_f) = \hat{\mathcal{C}}_{\mathbf{q}\omega} [\hat{P}(z_f)] = \exp \left[-i \frac{\kappa^2(\mathbf{q})}{2n(\omega)k_0(\omega)} z_f + ik_0(\omega) [n(\omega) - n_g] z_f \right] \quad (2.23)$$

where we have employed the substitution $k_0(\omega) = \omega/c$ for readability. It is easy to observe by inspection that a monochromatic plane wave in the form of Eq. (2.8), for which $\kappa^2(\mathbf{q}) = 0$ and the group velocity at ω_0 , $n_g(\omega_0)$, will remain unchanged during propagation in this moving reference frame, as expected.

Though this transform may seem like merely a small theoretical nuance, having the equation in this form has profound implications, and suggests that, if the

complete transformation $\hat{\mathcal{C}}_{\mathbf{q}\omega}$ of the input electric field $\mathbf{E}(z = 0)$ can be easily calculated, then solving the wave equation from Eq. (2.15), a partial differential equation, is as simple as point-wise multiplication in the spectral domain. In addition, this technique has the further advantage that its only source of error is associated with the transforms themselves, as opposed to finite-difference techniques like the Runge-Kutta family[27] for which the error scales with the step size in z and which require substantially more iterations, and therefore run time, to ensure accuracy.

Finally, leaving the propagation in the form of Eq. (2.23) is extremely useful for ultrashort pulse propagation. Given a continuous refractive index $n(\omega)$, its inclusion in the propagation equation properly handles all dispersive properties of the material without the need for cumbersome series expansions, as is often used to handle wave dispersion[5, 1]. Additionally, in other works, see Ranka and Gaeta[28], taking into account the frequency dependence of ultrashort pulses is often considered using Taylor expansions about the central frequency of the pulse. Not only does this add complexity and sacrifice accuracy, but this expansion only holds for pulses directly surrounding the frequency ω_0 of interest, and handling multicolored fields becomes difficult. The technique introduced here uniquely avoids these complications, by incorporating these effects in Eq. (2.23) with the continuous frequency-dependent wavevector $k_0(\omega)$.

2.1.2 Spatial Integral Transformations

Including the spatial phase contribution for a beam propagating in Cartesian free space, an XY geometry, is relatively simple, since the transverse Laplacian term is completely separable:

$$\nabla_{\perp}^2 = \frac{\partial^2}{\partial x^2} + \frac{\partial^2}{\partial y^2} \quad (2.24)$$

This can be solved by employing a 2-dimensional Fourier transform, one for each dimension of $\mathbf{q} = \{q_x, q_y\}$, so that

$$\hat{\mathcal{S}}_{\mathbf{q}} = \hat{\mathcal{F}}_{q_x} \circ \hat{\mathcal{F}}_{q_y} \quad (2.25)$$

The inverse operator is similarly defined. With this transformation, the phase term $\kappa^2(\mathbf{q})$ associated with the Laplacian operator, calculated using Eq. (2.18), is found to be

$$\kappa^2(\mathbf{q}) = q_x^2 + q_y^2 = \mathbf{q} \cdot \mathbf{q} = |\mathbf{q}|^2 \quad (2.26)$$

Note that, the definition of the q_x and q_y vectors in simulation code, like the definition of the frequency vector ω , will depend on the boundary conditions of the problem and parameters of the simulation.

If radial symmetry is included, so that a coordinate $r = \sqrt{x^2 + y^2}$ can be defined, the transverse Laplacian becomes more complicated

$$\nabla_{\perp}^2 = \frac{1}{r} \frac{\partial}{\partial r} + \frac{\partial^2}{\partial r^2} \quad (2.27)$$

Using spectral techniques to solve this equation involves finding a set of basis functions which are the eigenfunctions of Eq. (2.27). These functions are known to be the zeroth-order Bessel functions of the first kind[20], for which

$$\nabla_{\perp}^2 J_0(qr) = -q^2 J_0(qr) \quad (2.28)$$

In order to take advantage of this fact, a new integral transform must be defined, known as a Hankel Transform[30] $\hat{\mathcal{H}}_q$, which is a continuous transformation into Bessel-function space. The Sturm-Liouville orthogonality condition for the Bessel

functions of interest states³

$$\int_0^\infty dr r J_0(ar) J_0(br) = \frac{\delta(a-b)}{a} \quad (2.29)$$

which suggests that the transformation integrals are

$$\begin{aligned} \hat{\mathcal{H}}_q [f(r)] &= g(q) = \int_0^\infty dr r J_0(qr) f(r) \\ \hat{\mathcal{H}}_r^{-1} [g(q)] &= f(r) = \int_0^\infty dq r J_0(qr) g(q) \end{aligned} \quad (2.30)$$

This means that, transforming a function according to the relations in Eq. (2.30), letting $\hat{\mathcal{S}}_{\mathbf{q}} = \hat{\mathcal{H}}_q$ and recognizing that $\mathbf{q} = \{q_r\}$ is 1-dimensional, the spatial phase term is given by Eq. (2.28):

$$\kappa^2(\mathbf{q}) = q_r^2 = |\mathbf{q}|^2 \quad (2.31)$$

Notice that this term, rather unsurprisingly, mirrors the phase for the Cartesian geometry given in Eq. (2.26).

This derivation has so-far only discussed continuous transformations, but these conclusions still hold for transformations over discrete modes, as is necessary for propagation in photonic crystal structures such as the Kagome fiber. In this case, $\mathbf{q} \rightarrow m$ is an integer *mode index* and the eigenvalues $\kappa^2(m, \omega)$ may also be continuous function of ω , since the modal structure is strongly frequency dependent.

³The implementation in the code actually relies on a slightly different orthogonality condition, used in particular by Yu *et al*[34], though the principle remains the same. However, the key in this implementation is that the particular definitions of the r and q vectors satisfy the boundary condition that the field be identically zero at some desired radius, which can be set to that of a cylindrical capillary. Inside the radius, the modes still comprise a complete basis, which means that they are sufficient for propagation in an arbitrary radially symmetric geometry, so long as there is no field outside the chosen radius, which is already a condition for the model.

The spatial transformation to m -space involves calculating the modal content of the function of interest, done using the generalized inner product, which typically involves using an integral. For a mode $\mathbf{M}_m(\mathbf{x})$, which corresponds to mode index m , the time-dependent coefficient of the mode $E_m(t, z)$ can be calculated. Notice that the modes are, in general, vector valued so that they may store information about the polarization. Using Dirac notation to represent inner products, the coefficient is defined as

$$E_m(t, z) = \langle \mathbf{E}(\mathbf{x}, t, z) | \mathbf{M}_m(\mathbf{x}) \rangle = \int_{\mathbb{R}^2} d\mathbf{x} \mathbf{E}(\mathbf{x}) \cdot \mathbf{M}_m(\mathbf{x}) \quad (2.32)$$

The modes must satisfy completeness, so that a linear combination of the modes can create an arbitrary field in the domain of interest. In this case, so long as the modes are orthogonal to one another, the field can be reconstructed in terms of the mode coefficients

$$E(\mathbf{x}, t, z) = \sum_m \frac{\langle \mathbf{E} | \mathbf{M}_m \rangle}{\langle \mathbf{M}_m | \mathbf{M}_m \rangle} |\mathbf{M}_m\rangle = \sum_m \frac{E_m}{\langle \mathbf{M}_m | \mathbf{M}_m \rangle} |\mathbf{M}_m\rangle \quad (2.33)$$

In the case that the modes are normalized, the inner product term in the denominator, $\langle \mathbf{M}_m | \mathbf{M}_m \rangle$ is identically one[32].

For certain structures which require using modal decompositions for propagation, notably photonic crystal structures, an additional contribution to the refractive index from the different modes, and relatedly the loss, is often provided instead of $\kappa^2(\mathbf{q})$. This is merely a difference in notation, and makes no substantive difference in implementation. In particular, this work is interested in the properties of the Kagome-type hollow core photonic crystal fibers, which are characterized in more detail in Ch. 5.

Finally, in order to reduce the dimension of any of the equations in this section, so that they may be solved more efficiently by taking advantage of additional

boundary conditions or symmetries, such as considering only the on-axis field during propagation in a confining geometry, one must be particularly careful to include the transverse profile of the pulse, so as not to throw away relevant spatial information. This can be done by taking inner products of the beam profile with the modes of interest in the system, a procedure which is carried out in Sec. 5.1.

2.2 Field Conventions

At this point, it is important to discuss the relationship between the electric field and the intensity. For this report, the electric fields \mathbf{E} are represented as complex valued functions with the *negative frequency* convention, so that only the negative Fourier components are used to make up the field. In addition, the normalization is such that the intensity is defined so that

$$I = \frac{1}{2}\epsilon_0 nc|\mathbf{E}|^2 . \quad (2.34)$$

Representing the fields as complex vectors is convenient for the computational implementation, but the physical fields and material properties must be pure real for satisfying the physics. For the previous section, which concerned only linear differential equations, this is of no consequence, but, for nonlinear optics, having access to real valued quantities, denoted with a bar, is of critical importance. As such, it is important to define additional operators, $\hat{\mathcal{R}}$ and $\hat{\mathcal{R}}^{-1}$, which can transform the physical electric field $\bar{\mathbf{E}}$ to and from the complex field \mathbf{E} . The transformation operators are defined as follows:

$$\begin{aligned} \bar{\mathbf{E}} &= \hat{\mathcal{R}}[\mathbf{E}] = \Re[\mathbf{E}] \\ \mathbf{E} &= \hat{\mathcal{R}}^{-1}[\bar{\mathbf{E}}] = 2\hat{\mathcal{F}}_t^{-1} \left[\hat{\mathcal{F}}_\omega[\mathbf{E}] \cdot \Theta(-\omega) \right] \end{aligned} \quad (2.35)$$

where $\Re[A]$ is the real part of complex quantity A and Θ is the Heaviside theta function, which, combined with the Fourier operators, selects only the negative frequency components of $\bar{\mathbf{E}}$. The factor of 2 in the definition of \mathbf{R}^{-1} is for energy conservation. Notice that these operators are only inverses of one another so long as the field contains only negative frequency components, as is our convention.

The operators in Eq. (2.35) can be used for all of the other complex valued fields as well. In particular, the relationship between the real material polarization $\bar{\mathbf{P}}$ and the complex material polarization \mathbf{P} is particularly important in the next section, which concerns the nonlinear relationship between the electric fields.

2.3 Bound Nonlinear Optics

In Sec. 2.1, which concerned linear propagation, it was asserted that the material polarization \mathbf{P} demonstrates a linear relationship with the electric field, as in Eq. (2.6). However, at sufficiently high intensities, the physical polarization $\bar{\mathbf{P}}$ exhibits a nonlinear response to the physical electric field $\bar{\mathbf{E}}$. This is traditionally broken up into a power series in terms of the field[3] such that

$$\bar{\mathbf{P}}(\bar{\mathbf{E}}) = \bar{\mathbf{P}}_L(\bar{\mathbf{E}}) + \bar{\mathbf{P}}_{NL}(\bar{\mathbf{E}}) = \bar{\mathbf{P}}_L(\bar{\mathbf{E}}) + \epsilon_0 \hat{\chi}^{(2)} \bar{\mathbf{E}}^2 + \epsilon_0 \hat{\chi}^{(3)} \bar{\mathbf{E}}^3 + \dots \quad (2.36)$$

where $\bar{\mathbf{P}}_{NL}$ is the physical nonlinear polarization and $\bar{\mathbf{P}}_L$ is the linear polarization, defined by Eq. (2.6). The coefficients of the series $\hat{\chi}^{(n)}$ are the n th nonlinear susceptibility, which are, in general, frequency dependent and, as such, are operators in the temporal domain. Note that, though these nonlinear coefficients are, in general, tensors, this effect will not be studied in this report, and will not be considered.

Note that, as in Eq. (2.35), the stored nonlinear polarization \mathbf{P}_{NL} is obtained from the physical nonlinear polarization $\bar{\mathbf{P}}_{NL}$ by applying \mathcal{R}^{-1} . This means that

the added nonlinear contribution, for the positive frequencies, is given in terms of the stored electric field \mathbf{E} by:

$$\mathbf{P}_{\text{NL}} = \mathcal{R}^{-1} [\bar{\mathbf{P}}_{\text{NL}} (\mathcal{R}[\mathbf{E}])] \quad (2.37)$$

This is a critically important point, since only using the real electric field will give accurate results. With this additional term added to Eq. (2.15), we can write our wave equation as a first order differential equation in z in terms of a linear operator $\hat{\mathcal{L}}$ and a nonlinear operator $\hat{\mathcal{N}}$

$$\frac{\partial \mathbf{E}}{\partial z} = i \frac{\nabla_{\perp}^2 + 2\hat{n}(\hat{n} - n_g)\hat{k}_0^2}{2\hat{n}\hat{k}_0} \mathbf{E} + \mathbf{P}_{\text{NL}}(\mathbf{E}) = \hat{\mathcal{L}}[\mathbf{E}] + \hat{\mathcal{N}}[\mathbf{E}] . \quad (2.38)$$

It is prudent to know how to handle each of these operators in isolation from one another. Since solving the linear operator $\hat{\mathcal{L}}$ has already been discussed in Sec. 2.1, the remaining sections will concern the form of the nonlinear contribution,

$$\frac{\partial \mathbf{E}}{\partial z} = \hat{\mathcal{N}}[\mathbf{E}] = -\frac{i}{2\epsilon_0\hat{n}\hat{k}_0 c^2} \frac{\partial^2 \mathbf{P}_{\text{NL}}(\mathbf{E})}{\partial t^2} = \frac{i\hat{\omega}}{2\epsilon_0\hat{n}c} \mathbf{P}_{\text{NL}}(\mathbf{E}) , \quad (2.39)$$

under a variety of different circumstances.

2.3.1 Self-Phase Modulation

One of the simplest nonlinearities is known as self-phase modulation, which occurs when a monochromatic wave encounters a medium with a $\chi^{(3)}$ nonlinearity. For a

monochromatic plane wave, the physical nonlinearity $\bar{\mathbf{P}}_{\text{NL}}$ is given by

$$\begin{aligned}\bar{\mathbf{P}}_{\text{NL}} &= \epsilon_0 \chi^{(3)} \left[\frac{1}{2} E_0(z) e^{-i\omega_0 t} + \frac{1}{2} E_0^*(z) e^{+i\omega_0 t} \right]^3 \\ &\propto \frac{1}{8} [E_0(z)]^3 e^{-3i\omega_0 t} + \frac{3}{8} |E_0|^2 E_0 e^{-i\omega_0 t} + \frac{3}{8} |E_0|^2 E_0^* e^{+i\omega_0 t} + \frac{1}{8} [E_0^*(z)]^3 e^{+3i\omega_0 t}\end{aligned}\quad (2.40)$$

where E_0^* is the complex conjugate of E_0 , the complex field amplitude. Mediated by the nonlinearity, we generate contributions to two different frequency components at ω_0 and $3\omega_0$ respectively. Here, the wave at $3\omega_0$, known as the third harmonic, is not of interest and can be ignored. The contribution at the fundamental frequency, however, is called self-phase modulation.

Though the above derivation was done for a monochromatic wave, the same analysis holds for a pulse, in which $E_0(t, z)$ also displays some time dependence. In this case, the nonlinear contribution to our wave equation from Eq. (2.39) becomes

$$\frac{\partial \mathbf{E}}{\partial z} = -\frac{3i\chi^{(3)}\hat{\omega}}{8\hat{n}c} |\mathbf{E}|^2 \mathbf{E} . \quad (2.41)$$

The nonlinear contribution shown in Eq. (2.41) gives rise to self-phase modulation and self-steepening[11], in time, and self-focusing[28], in space. In addition, the frequency dependence of this effect brought about by the $\hat{\omega}$ operator introduces the effect of self-steepening[11] without any extra effort, whereas the incorporation of this term would otherwise require a Taylor series expansion about the central frequency[5, 28]. This simple representation easily allows for multicolored fields (typically known as cross-phase modulation), as the $\hat{\omega}$ term automatically selects and introduces the desired frequency dependence, along with a couple of small, yet often neglected terms with frequency $2\omega_1 - \omega_2$ and $2\omega_2 - \omega_1$.

2.3.2 Wave Mixing

In addition to self-phase modulation, which is inherently centered about a single frequency, the nonlinear polarization can couple between waves of different frequencies. In this case, the total electric field may be broken up into frequency regions and treated as separate, but overlapping pulses, as is a common practice for nonlinear wave mixing phenomena.

As for self-phase modulation, the coupled wave equations derived from including multiple input waves in Eq. (2.37) and Eq. can be shown to match those from other literature[5, 31]. However, our representation using the $\hat{\omega}$ operator means that the coupling process inherently satisfies conservation of energy and the frequency dependence, which is otherwise difficult to include[25].

Second harmonic generation occurs in a $\chi^{(2)}$ material when a wave \mathbf{E}_1 surrounding a frequency ω_0 couples to a field \mathbf{E}_2 with a spectral range centered at $2\omega_0$. In this case, the coupled wave equation are

$$\begin{aligned}\frac{\partial \mathbf{E}_1}{\partial z} &= \frac{i\hat{\omega}\chi^{(2)}}{2\hat{n}c} \mathbf{E}_2 \mathbf{E}_1^* \\ \frac{\partial \mathbf{E}_2}{\partial z} &= \frac{i\hat{\omega}\chi^{(2)}}{4\hat{n}c} \mathbf{E}_1^2\end{aligned}\tag{2.42}$$

Relatedly, the equations for four-wave mixing, which occurs for a $\chi^{(3)}$ material and $\omega_1 + \omega_2 = \omega_3 + \omega_4$, are shown to follow the same sort of pattern. This is true in general for wave mixing nonlinear effects.

2.4 Plasma and High Harmonic Generation

In addition to wave mixing nonlinearities, more intense effects can be modeled by the simulation. In particular, at very high peak intensities, such as those available in the Kärtner lab at MIT, plasma and its generation are of great interest. There

are a number of different avenues for creating plasma, in which electrons are stripped from their parent atoms. The lowest intensity method for creating a plasma is *multiphoton ionization*, in which multiple photons are simultaneously absorbed by an atom[8], in the process raising an electron above its potential well.

Instead of multiphoton ionization, the simulation package, which was designed with the intention of modeling extreme nonlinearities like high harmonic generation, implements *strong field ionization*. The ionization rate $W(\mathbf{E})$ is given by the well-known Ammosov-Delone-Krainov (ADK)[2] rate for tunneling ionization. In this report, the ionization rate is treated as being a function of the *physical* electric field $\bar{\mathbf{E}}$ because the sub-cycle dynamics are extremely important for calculating effects such as high harmonic generation. However, it should be noted that many expressions for the ADK rate are averaged over an electric field cycle, and instead take the field envelope \mathbf{A} as an input. To maintain generality in notation, the stored field \mathbf{E} is passed to W .

Though there are additional effects, such as recombination, avalanche ionization and multiphoton ionization, these are not of interest for the models in this work. Finally, since the rate of plasma formation depends only on the density of atoms which have not been ionized, the equation used for plasma generation is

$$\frac{\partial \rho}{\partial t} = W(\mathbf{E}) [\rho - \rho_n] \quad (2.43)$$

where ρ is the plasma density and ρ_n is the density of neutral atoms/molecules. Naturally, if multiple gasses are used simultaneously, this equation must be solved for each. Fortunately, none of these will couple to one another. Solving this simply requires assuming that the plasma is identically zero at the input of the pulse, and then integrating along in time. In addition, each point in space will have an independent solution for each time step. Finally, it is easy to see that, as the plasma ionization rate increases, the plasma density should asymptotically

approach the neutral density, as expected.

In addition, generating the plasma causes a loss of energy in the fields. Typically, this effect is quite small, but it is included for completeness. For a material with an ionization energy I_P , the ionization loss is given by

$$\frac{\partial \mathbf{E}}{\partial z} = -\frac{I_P}{2c\epsilon_0|\bar{\mathbf{E}}|^2} \frac{\partial \rho}{\partial t} \mathbf{E} \quad (2.44)$$

Notice that the term in the denominator is the physical field $\bar{\mathbf{E}}$, defined in Sec. 2.2. However, since the plasma would only be generated at the strongest point in the field, this distinction makes only a nominal difference.

Once the plasma has been created according to Eq. (2.43), the free electrons can interact with the electric fields, introducing additional nonlinear effects. In particular, an electron in an electric field experience an acceleration and, in turn, radiate. This causes changes in the electric field, which creates a contribution to the propagation equation that couples to the plasma density[13]:

$$\begin{aligned} \frac{\partial \mathbf{E}}{\partial z} &= -\frac{1}{2c} \int_{-\infty}^t dt' \omega_p^2 \mathbf{E} = -\frac{1}{2c} \int_{-\infty}^t dt' \frac{e^2}{m_e \epsilon_0} \rho(x, y, t', z) \mathbf{E}(x, y, t', z) \\ &= i \frac{e^2}{m_e \epsilon_0 \hat{\omega}} \rho(x, y, t', z) \mathbf{E}(x, y, t', z) \end{aligned} \quad (2.45)$$

where the plasma frequency ω_p is defined and depends on the plasma density $\rho(x, y, t, z)$. In addition, in the last line, the integration operator has been replaced with $(i\hat{\omega})^{-1}$, the inverse of the derivative, as a generalization of Eq. (2.18). Notice that, because of this replacement, the primary contribution of this term to the field is seen to be phase. In addition, for regions of high plasma density ρ , the contribution has a sign which is opposite to that of self-phase modulation. As a result, this effect will lead to *plasma defocusing* of the beam.

Finally, the extreme nonlinear effect known as High Harmonic Generation

(HHG) is also implemented, using the well-known *three step model*[7]. In this model, an electron is ionized from an atom, moves following a classical trajectory, and recombines with its parent nucleus. During its propagation it, under the semi-classical approximation, accumulates complex phase according to the action, which, upon interference with other electrons upon recombination, results in the generation of extremely high frequency electric fields, which occur at odd harmonic multiples of the driver frequency. The so-called single atom response, describes how the field can be generated by a single ionized and recaptured electron. This is calculated and multiplied by the density of neutral atoms to obtain the bulk material response to an intense field.

In addition to calculating the bulk material response, the rate at which electrons recombine with their parent atoms must be included. In the model discussed above, this is taken into account using quantitative rescattering (QRS) theory[21]. Lastly, the implemented version of high harmonic generation only correctly handles fields which have a single central frequency peak, which improves speed, though HHG for multi-colored fields is currently under development.

Chapter 3

Numerical Package Architecture

Most simulation codes for nonlinear optical propagation follow the basic split-step-Fourier structure shown in Alg. 1. Typically, this consists of a set of function and parameter definitions based upon material properties and experimental conditions, followed by a loop which iteratively converts between the spectral and real-space domains and calculates the effects of the linear and nonlinear contributions to propagation[1].

For simple modifications such as switching the propagation material, which affects the refractive index, not much change is needed, and if the swap is sufficiently frequent, `if-else` statements are often used to make this even simpler. However, what happens if the nature of the nonlinearity is changed? Or a new nonlinear effect is added? These modifications are not so trivial. Even more compelling is the case of nonlinear wave mixing, in which the number of interacting pulses is not necessarily fixed during propagation. Such a switch would require almost a complete modification of the model. The complexity of the code grows quickly with the number of desired alterations, and, as experimental configurations change, reusing blocks of code becomes increasingly difficult, even though the numerical techniques for solution may remain the same.

Algorithm 1 Simple Split-Step Propagation. The main propagation routine iteratively applies the linear operator (in the spectral domain) and the nonlinear operator (in the real domain).

```
1: ▷ Initialize the parameters and use them to define the field
2: PropagationParameters ← SetParameters ()
3: PulseField ← InitializeField (PropagationParameters)
4:
5: while z < zMax do           ▷ Loop until propagation reaches end condition
6:   ▷ Linear Propagation (by step size dz)
7:   SpectralField ← TransformToSpectralDomain (PulseField)
8:   SpectralField ← ApplyLinearOperator (SpectralField, dz)
9:   PulseField ← TransformToRealDomain (SpectralField)
10:
11:  ▷ Nonlinear Propagation (by step size dz)
12:  PulseField ← ApplyNonlinearOperator (PulseField, dz)
13:
14:  z ← z + dz                  ▷ Update z position
```

To address this ubiquitous complication, we present a code which is designed with a higher level of abstraction than the typical optical pulse propagation simulation described above. It aims to provide a simple scripting interface for creating easily modified and reusable code. This section of the thesis is devoted to a description of the framework underlying this simulation package, along with a set of benchmark test uses. Subsequently, it will be used for a more in-depth analysis of a number of nonlinear phenomena, including modulational instability in photonic crystal fibers and high harmonic generation.

In order to ensure that the code package is useful for an array of different experimental configurations, the methods for calculating pulse propagation must be encapsulated into functions which can be called on-demand. In addition, these functions, particularly those for nonlinear wave mixing, must scale to support an arbitrary number of input pulses, each presumably centered about its own central frequency. Finally, modularity is an asset if the package is to be used for different experiments. With this in mind, the code must be structured in such a way that

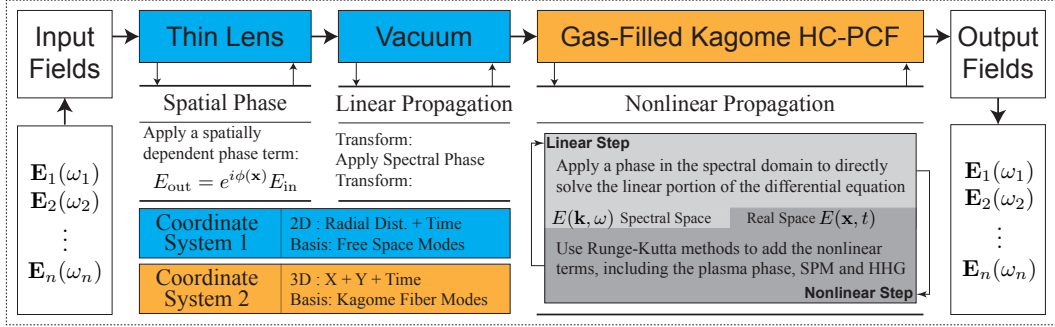


Figure 3-1: Schematic showing an example simulation, which corresponds to an experiment to study nonlinear optics in a Kagome hollow core photonic crystal fiber. In the setup, an optical waveform is focused into a gas-filled Kagome fiber, which, in the model, requires propagating the pulse through the focusing optic and vacuum before it reaches the fiber itself.

additional effects can be easily incorporated without modification of the overall design.

All the above features are best realized using an object-oriented design. As such, the pulse propagation package presented here is programmed in MATLAB[24] using its object-oriented functionality. Not only is MATLAB a pervasive tool in many research environments, but MATLAB is platform independent and has extensive features for parallelization and GPU acceleration for matrix operations. In addition, MATLAB, while powerful, is relatively easy to use and comes installed with many functions for plotting and data management. This allows the code to be easily used in almost any laboratory.

Shown in Fig. 3-1 is an example schematic which illustrates these ideas. In particular, notice that field objects are passed between optical components, which, in turn, modify the fields according to their propagation equation. For the thin lens, a simple optical element, a spatially dependent phase is applied to the input fields. However, for the gas-filled Kagome HC-PCF, the full nonlinear propagation equation must be solved, since an analytic expression is not available. In addition, notice that the numerical representation of the pulses, defined by the coordinate

system objects, can change between elements. This allows for more efficient simulations, which are capable of exploiting symmetries in the experiment.

A large portion of this thesis is devoted to the implementation of the theory of nonlinear optical pulse propagation in the code. In the previous chapter, it was briefly discussed how the theories outlined there can be translated into numerical techniques, but this is only a piece of the simulation package presented here. This chapter is devoted to outlining the structure of the code alongside a motivation of its use. Section 3.1 outlines the class structure of the simulation, being sure to highlight the most significant classes and those which can be subclassed to extend the functionality of the package. Section 3.2, will describe in detail the steps the code undergoes to model the propagation of a pulse subject to nonlinear effects. This includes a discussion of how data is passed between the different elements. Finally, Sections 3.2.2, and 3.2.3, detail how nonlinearities and high harmonic generation are implemented, and how more effects can be easily added by the user.

3.1 Class Hierarchy

Here we introduce the class structure for our numerical package. Nearly all classes in the package derive from a single `npObj` class which consists mostly of a name generator so that all objects are ensured a unique name, which is important for saving and loading data.

3.1.1 Data Manager [`npDataManager`]

The Data Manager, `npDataManager`, provides the main interface between the user and the remainder of the package. After initialization, which will be shown in more detail in the next chapter alongside demonstrations of the code, this object is

supposed to contain all of the data relevant for calculating the effect of propagation on the electric fields. Consequently, the data manager has parameters including `field` and `element` which are MATLAB cell arrays of fields, `npField`, and optical elements, `npEle`, respectively. In addition, the data manager contains the ‘master’ `propagation` function, which, when called, propagates the electric field objects through all of the different elements created by the user. More details on the specifics of propagation are in Sec. 3.2 on the Propagation Control Flow.

One of the most important functionalities of our package is its ability to save and load data with simple commands. Saving all of the data during propagation is often neither practical nor necessary. As such, the `npDataManager` has an easy-to-use yet powerful system for saving data during propagation which allows the user to easily customize what data is stored. In addition, often only a section of the data (e.g. the on-axis field) is needed for analysis after propagation. As a result the `load` command built into the `npDataManager` is capable of efficiently retrieving subsets of the saved data. The data manager delegates most of the saving/loading functionality to the `npSlice` object, the details of which can be found in the documentation in the code. However, the best way to learn how these functions work is by looking at examples, which can be found in the sample code provided with the package.

3.1.2 Coordinate System [`npCoord`]

The coordinate system and its subclasses store information regarding the coordinate axes (e.g. x , y and t) associated with the electric field data. In addition, not only does this object store geometrical data about the system (i.e. the core radius of a cylindrical capillary) but it is also designed to handle the conversion of the field data back and forth between its spatial and spectral representations, which are important for linear pulse propagation. On its own, however, the `npCoord`

element has almost no functionality, but is the superclass for more specific situations.

The most used incarnation of the coordinate system is in the child class `npCoordE`, which is meant to specifically handle electric field objects. This class supports an almost arbitrary input dimension. Maximally, a full 3D pulse can be simulated in xyt -space, but it is often advantageous to exploit some symmetries (e.g. radial) so that $xy \rightarrow r$ can be used. In some geometries, in fact, including the hollow cylindrical capillary, this symmetry is required, so that the field is identically zero along the boundary. The full capabilities of this feature are better understood with examples, such as those provided in Ch. 4. Coupled with supporting arbitrary dimension input, the `npCoordE` class also automatically takes care of transforming the pulse into the spectral domain, which as was shown in Sec. 2.1.2 relies heavily on the geometry of the input. Finally, the `npCoordE` also supports transformations into an arbitrary set of orthogonal basis profiles, and, as such, can support propagation through photonic crystals, for which such a step is necessary. More specific details concerning implementation can be found in the documentation.

In addition, the `npCoord` object was designed with the intent of supporting an `npCoordH` subclass, which is used for high harmonic generation. Like `npCoordE`, the `npCoordH` has coordinate vector functions for the dimensions of interest (including time and the different spatial coordinates). By contrast, the high harmonic generation needs only to be stored for a limited number of points, since calculating the HHG for each point on the grid can be extremely computationally expensive. As such, a separate cell array of indices which define the points in another coordinate system for which the HHG is calculated. Relatedly, the `npCoordH` must be defined with a *parent* `npCoordE` coordinate system, to which these indices correspond.

3.1.3 Field [npField]

The field object, `npField`, and its subclasses store the electric field tensor and other related meta-data, such as the initial conditions on the energy or pulse duration. Like the `npCoord` object, this class provides very limited functionality on its own, but defines a handful of abstract methods which are in turn defined by the subclasses. In particular, there are a number of helper functions associated with the `npField` subclasses which make it easier to calculate important field properties such as the intensity and energy. Furthermore, each of the subclasses has overridden versions of popular functions, including basic algebraic operations, the fast Fourier transform, etc. This allows one to easily manipulate the field functions and then pass them as arguments to the primary methods in the code without having to worry about many of the specific details.

The most frequently used subclass is the `npFieldE` class, which is used for a majority of ultrashort pulses. It stores the field in its `field` parameter as a 4D tensor, with dimensions corresponding to, space (of which there are always 2, even if one or both are degenerate), time, and polarization. In addition, there is a separate field for the frequency `w`, which returns either the ω vector, if the field is stored as a function of time, or the central frequency ω_0 , if the field is stored as a single profile. Note that, because of the negative frequency convention, the central frequency component of the electric field occurs for $\omega < 0$. To maintain consistency for functions pertaining to propagation, this also requires that the `w` function return a negative term, $-|\omega_0|$, for fields without any temporal extent. Details of the steps during propagation are given in the next section.

For high harmonic generation, the `npFieldH` class is typically used. Other than possessing a `npCoordH` coordinate system as opposed to an `npCoordE`, the `npFieldH` is not dramatically different from the `npFieldE`; it contains a number of functions for calculating the derivative properties of the field such as

the spectrum and the total energy. In addition, like the npCoordH from the previous section, the fields are stored in a 2D array, with each row corresponding to a particular point in space of an associated npCoordE.

3.1.4 Optical Material [npMat]

The material in which the pulse is traveling is critical for determining propagation dynamics. The npMat class is the superclass which represents any of the variety of materials through which the light will propagate. As such, the class provides a number of abstract methods including the refractive index n and a number of nonlinear parameters as well ($\chi^{(2)} \rightarrow X2$ and $\chi^{(2)} \rightarrow X3$). These methods are then called by the linear and nonlinear propagation functions, described below.

Adding a new optical material is relatively simple, as only the significant properties of a material need to be added by the user, to the functions outlined in the documentation, through *class overloading*. If no value is given, for the refractive index for example, the value for vacuum is used.

3.1.5 Optical Element [npEle]

The optical element objects effectively tie everything together. Each optical element provides a specific `propagate` function, which, as the name would imply, calculates the output electric fields from the input electric fields using the propagation equation associated with the physical object. Each element in the code corresponds to a physical element in the optical system through which the fields are propagating. For example, in the case of Fig. 3-1, a set of input fields passes through a thin lens (`npEle 1`), propagates in vacuum (`npEle 2`) and is finally guided by the Kagome fiber (`npEle 3`).

Each of these simulated objects typically has its own coordinate system, which means that a prerequisite of the `propagate` method is that the coordinate sys-

tems of the electric field objects must be set to match. As such, when the fields are passed from one element to the next, the stored fields must be interpolated, if necessary, to match the new coordinate system. This process also takes care of including the coupling coefficients into the new element, when applicable. In the case of the example above, this interpolation is necessary when the fields are passed between the vacuum and the Kagome fiber. Since the dimensionality of the coordinate systems changes from possessing radial symmetry to storing the entire 3D fields, matrix which represents the fields in the vacuum must be ‘spun’ about the central axis to generate the new representation.

Perhaps the most important subclass of `npEle` is the nonlinear optical element `npEleNonLin`, which is, itself, a subclass of the linear propagation element `npEleLin`. The nonlinear element, which is used to model the Kagome fiber in Fig. 3-1, directly solves the nonlinear optical wave equation in the presence of a host of different nonlinear effects, namely those addressed in the previous chapter. This will be discussed in further detail in the remaining sections.

3.2 Propagation Control Flow

Upon initialization of the aforementioned objects, the user may call the `propagate` function of the `npDataManager` object `DM` they’ve created. A call to `propagate` loops through all of the `npEle` objects stored in the cell array `DM.element` and calls the function `propagate` associated with each of them. This represents how the beam propagates through the system; as the laser pulse propagates, it passes from one object to the next and is modified according to its properties, which can vary rather dramatically. As a matter of convenience, beam properties of interest are saved before and after the element’s propagation function is called, which allows for a direct look at how it modifies the laser beam.

Notice that the behavior introduced here is inherently much more flexible

than that of a basic nonlinear propagation solver, as in Alg. 1. For the package introduced here, more sophisticated behavior than propagating through a single element is supported, which is essential, for example, in modeling experiments of high harmonic generation, in which the nonlinear distortions of the beam before entering the target region can dramatically change the output. A structural model of a simulation like this can be seen in Fig. 3-1, which shows how the fields pass between the different elements.

For many elements, such as that of a thin lens, the propagation method is quite simple, consisting of only a multiplication of a spatially-dependent phase. However, many others involve directly solving differential equations for propagation, and cannot rely on analytic solutions. Here, these elements are referred to as *full-propagation* elements, of which there are three: `npEleLin` for linear propagation, `npEleNonLin` for nonlinear propagation, and `npEleHHG` for high harmonic generation (note that these classes are sub-classes of one another in this order). For the `npEleHHG` element, the propagation method follows the structure shown in Alg. 2. Notice that this and the more basic solver are structurally similar, since both rely on the split-step Fourier family of techniques to solve the differential equation for propagation, but keep in mind that each of the steps here are designed to support arbitrary numbers of field objects and have much greater flexibility.

3.2.1 Linear Propagation Step

The linear propagation portion of the code, which can be found in the `linearStep` method of the `npEleLin` class, is again rather similar to the procedure of the simple split-step Fourier technique from the beginning of the chapter. The `linearStep` function calls the `linearStepFieldE` and `linearStepFieldH` functions for, respectively, the electric field `npFieldE` and high harmonic field `npFieldH` ob-

Algorithm 2 Propagation flow for the most general full-propagation element: npEleHHG, which is capable of solving for linear and nonlinear propagation effects and the generation of high harmonics. Notice that it is structurally similar as Alg. 1, but there is a large amount of functionality which is effectively hidden from the user.

```
1: while z < zMax do      ▷ Loop until propagation reaches end condition
2:   LinearStep (DataManager, z, dz)
3:   NonlinearStep (DataManager, z, dz)
4:   HighHarmonicGenerationStep (DataManager, z, dz)
5:   SaveData(DataManager, z)
6:   z ← z + dz
```

jects. In each, the fields are transformed using the `fTransform` methods from their appropriate coordinate system objects (`npCoordE` and `npCoordH`).

After transformation, the fields are multiplied by the propagation operator, which is calculated for each of the fields. For typical electric field objects, the propagation operator is calculated using the `calcPropOperator` method of the propagator `npEleLin` object. The method simply calculates the operator defined in Ch. 2, however, it also contains a number of operations which cache the result to avoid calculating the costly object multiple times. The logic for calculating the propagation operator for high harmonic generation is far simpler (since the geometry is far less important of a concern), so the operator is directly calculated in the `linearStepFieldH` function.

Once the propagation operator is applied, the fields are transformed back once again, and the fields are passed to the nonlinear portion of the code.

```

1 function dEdz = ThirdHarmonicGeneration(self,z,F,nle)
2 % Inputs:
3 %   z    : position of pulse (um)
4 %   F    : cell array of npFieldE objects
5 %   nle : parameter data structure
6
7 % Parameters
8 P = npPhysicalConstants;           % Physical constants
9 g = nle.g;                      % Geometric
10 X3 = self.mat.X3(z);            % Nonlinear susceptibility
11 w = nle.w;                     % Frequency 'getter'
12 n = @(ppp) self.mat.n(w(F{ppp}),z); % Refractive index 'getter'
13
14 % Fundamental Field Change
15 dEdz{1} = nle.NL(...%
16     -3e-6i*X3.*w(F{1})*g/P.c./n(1)/8,...%
17     F{2}.*conj(F{1}).*conj(F{1})...%
18 );
19 % Third Harmonic Field Change
20 dEdz{2} = nle.NL(...%
21     -1e-6i*X3.*w(F{2})*g/P.c./n(2)/8,...%
22     F{1}.*F{1}.*F{1}...%
23 );
24
25 end

```

Listing 3.1: An example definition for a wave mixing nonlinearity function, defined in the `npEleNonLin` class. The structure of the method is extremely simple and, aside from parameter definitions, the set of coupled differential equations which are to be solved consist of only a few lines. It is easy to see that, by using the pre-defined `nle.NL` function, including custom wave mixing nonlinearities is extremely simple for even inexperienced users.

3.2.2 Nonlinear Propagation Step

The nonlinear step is a bit more involved than the linear step, but the basic principle is same; the data manager object is fed into the `nonlinearStep` function, which is defined in the `npEleNonLin` class. There are a host of supported nonlinear effects which can be included by the user. This is done by setting the `N` parameter in the input structure used to define the full-propagation element (see

the sample code and documentation for more details). Each nonlinearity specified is looped over and the contribution of those effects are added in sequence. As with any of the nonlinear effects, the result should converge to the physical solution as the step size is decreased. An adaptive step size has not been implemented (because of general unreliability in ensuring accuracy), so it is left to the user to determine when the solution has converged.

The largest class of nonlinear effects are the wave mixing nonlinearities, in which a nonlinear susceptibility results in an interaction between fields of different frequencies. These nonlinear effects all follow the same basic format. As such, the `npEleNonLin` class has a wrapper function, called `genWaveMixing`, which handles most of the sophisticated behavior necessary for modeling, including the definition of various helper variables and the numerical integration¹. With this wrapper function `nle.NL` (which is defined in the code), the definition of custom wave mixing nonlinear effects is extremely simple. One such effect, that of third harmonic generation, is shown in Listing 3.1. It is clear that translating the coupled equations for this process into the simulation code is simple when the `nle.NL` function is used. By customizing the nonlinear effects to suit one's needs, the user can efficiently simulate arbitrary wave mixing nonlinear effects.

In addition to the wave mixing nonlinearities, plasma nonlinearities are also considered. This is broken up into two different classes of functions: the plasma generating functions, which simulate how the plasma is created by the fields, and the plasma effect functions, which handle how the created plasma then affects the fields. The plasma generating functions are called when required and are inserted into the list of nonlinear effects directly before the first plasma effect function. The plasma generating functions, which, for the time being, includes only ADK

¹The numerical integration is carried out by a separate .m file, `npRK4`. In this file is an implementation of the popular Runge-Kutta[27] algorithm. However, it is designed to support MATLAB cell array input, which is necessary for supporting arbitrary numbers of coupled differential equations.

ionization[2], are defined with `npSingleGas`, since only ionization of gasses is supported.

Once the plasma is calculated, the densities are passed to the different plasma functions. The implementation of these is relatively straightforward (and the `PlasmaShift` function takes after the wave mixing nonlinearity conventions). The motivated reader is encouraged to look at the code for more details.

3.2.3 High Harmonic Generation Step

The high harmonic generation step is defined in `HHGStep` in the `npEleHHG` class. The overall structure is rather similar to that of the `nonlinearStep`, but the code had become rather difficult to understand, thereby necessitating the creation of a new class. As in the last section, the `HHGStep` function loops through the `hhgEffects` array, which can be set using `H` of the input structure to the element. Currently, only a limiting case of the three-step-model code is complete, in which only a single driver field is used.

The three-step-model calculation, appropriately handled by the `HHG_ThreeStepModel` method, loops through each point in space for HHG calculation. Since, for the three step model, the HHG is assumed to depend only on the field as a function of time, each point in space can be treated as independent. As such, each spatial point is sent to a separate *single atom response* (SAR) method, which takes in an electric field vs. time and returns the contribution to the HHG. In the included version of the code, the SAR code has not been included, as the best way to perform this calculation will depend on the user's preference and goal. It is left to the user to provide this method. The defined SAR function should return the electron acceleration, from which the field can be calculated in `HHG_ThreeStepModel`.

Finally, the frequency dependent recombination amplitude is obtained from the

`npSingleGas` objects from which the plasma was calculated. The recombination amplitudes are taken from file. See the implementation for details.

Chapter 4

Simulation Experimental Results

This chapter is devoted to providing some example simulations and code snippets for which the solution is either analytically known or the expected behavior is well understood. In addition, small excerpts of sample code will be sporadically included as necessary for understanding how the configuration files should be structured. All code required to reproduce the plots will not be included here, however, the test files included with the code contain nearly everything necessary to reproduce these results. Though many of the sections are well-established results, showing them here is important for demonstrating how the simulations work in practice. By contrast, the final section, which concerns high harmonic generation in a gas-filled cell, is a subject of active research, thereby showing that the simulation package has more sophisticated use cases.

4.1 Vacuum Linear Propagation

The simplest case of propagation is that of linear propagation. In particular, since the solution for propagating a CW Gaussian beam is analytically solvable, it is that case which shall be simulated first. The code for initializing and propagating

a Gaussian beam through vacuum is as follows:

```
1 % Coordinate System [ Free Space Propagation ]
2 iC.dim = 'XY';
3 iC.xM = 500; iC.xN = 1024;
4 iC.tM = 200; iC.tN = 2048/4;
5 iC.geometry.name = 'FreeSpace';
6 iC.name = 'FreeSpace';
7
8 % Field Parameters
9 iE.waist = 20;
10 iE.energy = 1;
11 iE.tau = 20;
12 iE.wavelength = 2.000;
13
14 % Element Definition
15 iM.name = 'VacuumElement';
16 iM.Z = [0,1000];
17 iM.dzM = 100;
18 iM.save = {'field','intensity'};
19
20 % Initialization
21 C = npCoordE(iC);
22 E = npFieldE(iE,C);
23 M = npEleLin(iM,C);
24 DM = npDataManager(E,M);
25
26 % Propagate
27 DM.propagate();
```

The elements (`npCoordE`, `npFieldE`, `npEleLin` and `npDataManager`) are all defined in sequence and then initialized using the appropriate constructors. After initialization, the `propagate` method of the data manager object is called, which, following the control flow outlined in Sec. 3.2, propagates the field in steps of $100 \mu\text{m}$ from 0 to 1 mm. At each of these points, the fields are stored, in accordance with the `iM.save` parameter. These can be easily plotted and compared with the analytic solutions. This is shown in Fig. 4-1 for both the input pulse at 0 mm and at the output pulse at 1 mm. It is clear that, though the error between the analytic solution and the simulated solution grows at the output from merely numerical noise at the input, the magnitude of the noise is

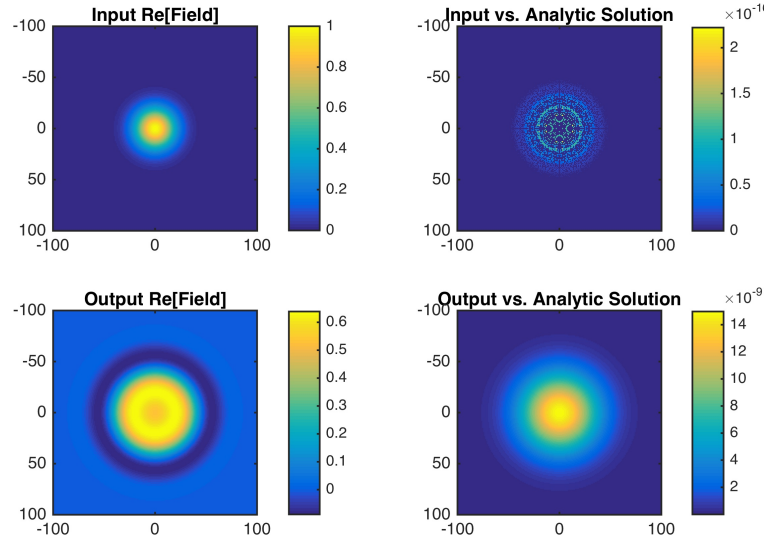


Figure 4-1: Example propagation of a Gaussian beam through vacuum, to demonstrate the basic capabilities of the simulation package. As expected, the beam, which starts in a collimated state, has diffracted at the output and is both larger and has a non-flat phase profile. Notice that the beam matches the analytic solution extremely well, showing errors only on the order of 10^{-8} at the output.

sufficiently low as to be ignored, confirming the accuracy of the linear portion of the propagated model. It should also be pointed out that though the dimension of the problem was set to be `iC.dim = 'XY'` (using the x and y coordinate axes), the code will also work as expected if this line is replaced with `iC.dim = 'R'`, for which radial symmetry is used and the Hankel transform, as introduced in Sec. 2.1.2, is employed. The results suffer imperceptibly in accuracy, yet can be computed substantially faster.

4.2 Nonlinear Self-Focusing

Nonlinear self-focusing is a self-phase-modulation-related effect. Including nonlinear effects involves only a handful of changes. First, the gas must be created and included in the initialization for the propagation element. Then, the nonlinear effect must be added as well. The additions/changes to the code will look as

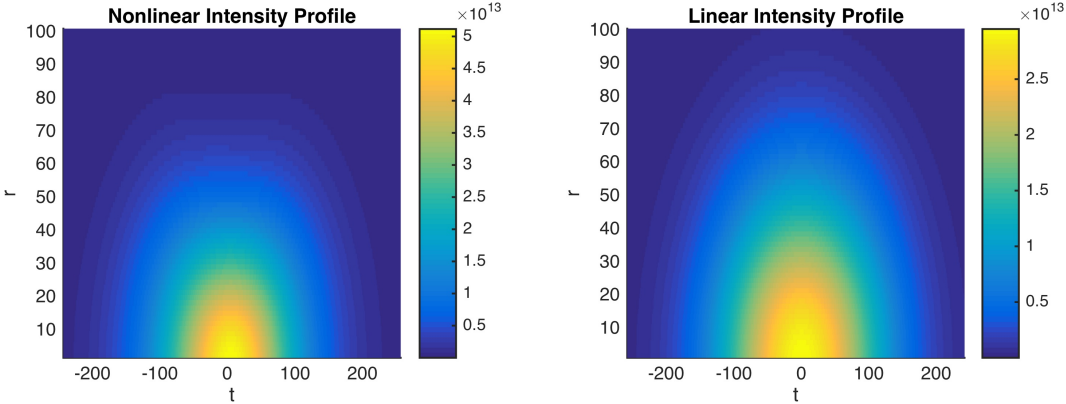


Figure 4-2: Propagation of a gaussian pulse at high energies through a nonlinear medium (10 bar of Argon gas) on the left, and without any nonlinearities on the right. This shows how self-phase modulation can cause self-focusing behavior. The center of the pulse on the left is far stronger at the output in the presence of the nonlinear response during propagation. The colorbars are in units of $\text{W}/\text{cm}^2 \text{o}$.

follows:

```

1 iM.N = 'SelfPhaseModulation';
2 iG.mat = 'Ar';
3 iG.P0 = 10;
4 G = npMatGas(iG);
5 M = npEleNonLin(iM,C,G);

```

The result from this propagation is found in Fig. 4-2. The plots show that, after propagation, the most intense portion of the pulse, centered at $t = 0$, has resisted diffraction, a signature of self-focusing. In particular, the peak intensity of the pulse is dramatically higher than that of the linear case, also shown. Finally, changing the dimension from RT to simply R will model the propagation of the on-axis field. Since the dispersion during propagation is relatively minor, eliminating the T field will yield the same result as the $t = 0$ cross section. In addition, the plotting functions are set-up so that they will continue to work as expected, even after this change is made.

4.3 Degenerate Four Wave Mixing

Nonlinear wave mixing is a useful technique for obtaining and amplifying optical pulses across frequencies. Despite the power of the technique, phase matching, which is a measure of the relative group velocities between the waves, is a universally important concern if the efficiency of the conversion process is to be maximized. There are a number of available techniques to enhance phase matching, including critical and quasi-phase matching (typically for second order nonlinear processes), but these almost necessarily use nonlinear crystals, which are subject to damage.

It is desirable, in many cases, to use a gas, for which the strength of the nonlinear interaction can be tuned as a function of the pressure. However, excluding regions of anomalous dispersion, perfect phase matching in a free-space gas is impossible. For this reason, this model will concern the propagation of a gas through a hollow core fiber, which is capable of imparting a phase on the optical pulses passing through it[23, 9], thereby allowing a phase matching condition which can be tuned by the gas pressure[12]. Here, the phenomena of degenerate four wave mixing will be discussed, a process in which the pump pulse provides two photons which are parametrically amplified into two generated photons at signal and idler frequencies. For a *zero-dimensional* wave (which is both a plane wave and continuous in time), the coupled equations for this behavior is as follows:

$$\begin{aligned}\frac{\partial E_p}{\partial z} &= -i \frac{2g\omega_p}{8n(\omega_p)c} \chi^{(3)} E_p^* E_s E_i , \\ \frac{\partial E_s}{\partial z} &= -i \frac{g\omega_s}{8n(\omega_s)c} \chi^{(3)} E_p^2 E_i^* , \\ \frac{\partial E_i}{\partial z} &= -i \frac{g\omega_i}{8n(\omega_i)c} \chi^{(3)} E_p^2 E_s^* .\end{aligned}\tag{4.1}$$

where g is a geometric factor (equal, in this case, to roughly 0.5655), described in

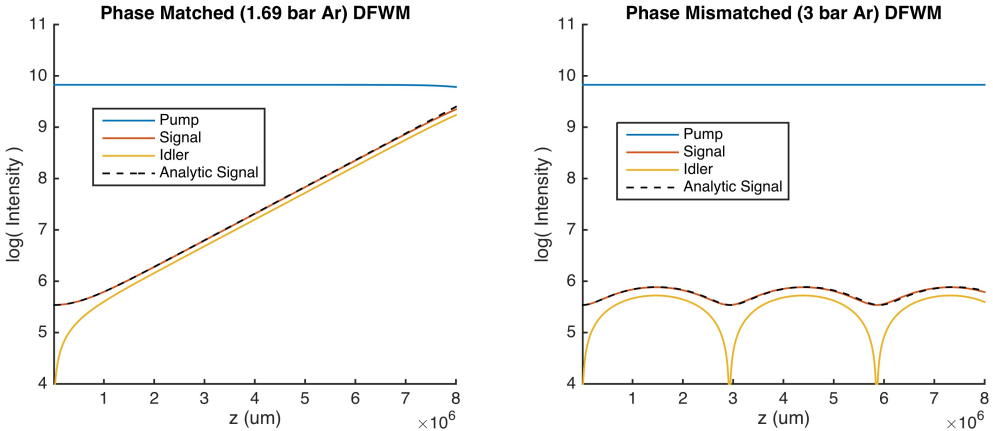


Figure 4-3: Examples of degenerate four wave mixing for phase-matched (left) and non-phase-matched (right) gas pressures. Notice that the analytic expression, shown as the black, dotted line in both plots, matches the signal field extremely well. While, when the process is phase matched, the signal and idler fields grow exponentially during propagation, the non-phase-matched system experiences back-conversion to the pump, which occurs when the G factor is imaginary.

more detail in Sec. 5.1.

One important consideration to keep in mind when analyzing the nonlinear mixing of waves, is that the propagation phase between the waves will change as a function of the carrier frequency. This means that, while two pump photons will constructively produce signal and idler photons for a period of time, eventually, the phase between the driving wave will shift with respect to the others. This process results in the creation of photons that are out of phase from the original generated photons, causing a destructive interference-like phenomena. This shift in phase of the different waves, known as a *phase mismatch*, is simply given by the sum in the propagation constants associated with the waves, with a combinatoric factor and sign determined by energy conservation. Knowing this, the wavevector mismatch (which is proportional to the phase mismatch) may be defined for the

lowest order fiber mode:

$$\begin{aligned}
\Delta k_1 = & 2P_1(\omega_p) - P_1(\omega_s) - P_1(\omega_i) \\
= & 2\sqrt{[n(\omega_p)k_0(\omega_p)]^2 - \left[\frac{u_{01}}{R}\right]^2} \\
& - \sqrt{[n(\omega_s)k_0(\omega_s)]^2 - \left[\frac{u_{01}}{R}\right]^2} \\
& - \sqrt{[n(\omega_i)k_0(\omega_i)]^2 - \left[\frac{u_{01}}{R}\right]^2}.
\end{aligned} \tag{4.2}$$

There is a simple analytic solution to an approximate form of the *zero-dimensional* wave equation in which the pump wave E_p is undepleted, or constant. The solution is written in terms of Δk_1 as follows[3]:

$$E_s(z) = E_s(0) \left[\cosh(Gz) - i \frac{\Delta k}{2G} \sinh(Gz) \right], \tag{4.3}$$

where $E_s(z = 0) \neq 0$ is the input signal field and, for the idler wave, $E_i(z = 0) = 0$. Also, the gain constant G is

$$G = \sqrt{E_p^4 \frac{g^2 \chi^{(3)}^2}{64c^2} \frac{\omega_i \omega_s}{n_i n_s} - \frac{\Delta k^2}{4}}. \tag{4.4}$$

The simulation code is capable of taking all of this into account. Zero dimensional fields are supported for just this purpose: checking that the coupled differential equations are behaving as one would expect. Simulations of a phase-matched case and a non-phase-matched case are shown in Fig. 4-3, which shows the nonlinear conversion of the fields alongside the analytic solution. In the phase matched system, the exponential growth of the signal and idler fields expectedly continues throughout propagation. By contrast, the non-phase-matched system, which is detuned by augmenting the gas pressure, experiences backconversion, displaying oscillatory behavior which occurs whenever the G factor defined in Eq.

(4.4) is imaginary, thus turning hyperbolic sine and cosine into their traditional trigonometric counterparts. Once again, this demonstration shows how simple it is to add sophisticated nonlinear wave-mixing effects to the simulated model.

4.4 Mid-Infrared Driven High Harmonic Generation

While it's certainly nice to know that the simulated model is capable of reproducing analytic results, realistic experiments are often more complicated, and understanding which nonlinear effects play an important role in the propagation dynamics is a motivating factor for more sophisticated simulations.

The Kärtner group at MIT has a cryogenic Yb:YAG laser which is capable of generating 50 mJ pulses at a 1 kHz repetition rate at 1 μm . This pump laser has an array of proven applications which include the generation of strong fourth-harmonic pulses for the creation of a ps deep-ultraviolet source[6] and the creation of 2.1 μm pulses through a multi-stage OPCPA[18]. In addition, this multi-stage OPCPA generates pulses which are powerful enough to be used for experiments in high harmonic generation [HHG]. For this particular experiment, a 6-mm-long cell is filled with 0.2 atmospheres of argon gas, which acts as a nonlinear and high harmonic gain medium. The driver pulses are focused to a beam waist of 60 μm , a duration of 45 fs and an energy of 600 μJ . These parameters correspond to those used in a related experiment, the goal of which was to maximize the high-harmonic generated photon flux surrounding the 150 eV range.

In the simulations, the perturbative nonlinearities which must be considered are self-phase modulation, plasma-phase shifts (which in-turn causes defocusing and blue-shifting), plasma ionization loss and inverse bremsstrahlung loss. Finally, the the high harmonic generation is calculated using the well-known three step

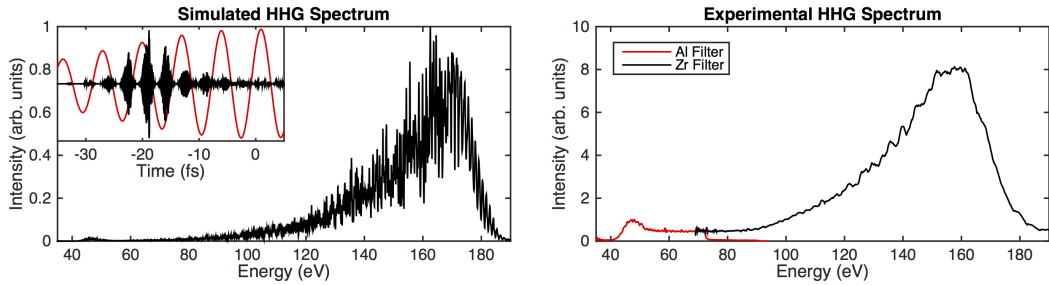


Figure 4-4: Results from a recent experiment at the Kärtner group at MIT alongside the corresponding simulations. The plots show the photon flux as a function of the photon energy. There is clearly good agreement between the two cases. The inset in the left plot, which shows the simulated spectrum, shows the attosecond pulse train (black) superimposed on the input driver electric field.

model, as was outlined in Ch. 2. The results from the simulation can be seen alongside those from the experiment in Fig. 4-4. The experimental results show that 2×10^8 photons/s were generated over a 1% bandwidth centered at 160 eV[18]. The results of the simulation clearly match the experimental results very well, reproducing, not only the high harmonic cutoff photon energy, but also matching locations of the maximum spectral peak. Finally, the simulations reveal information which is otherwise extremely difficult to ascertain in experiments. In particular, experimentally obtaining the attosecond pulse train which is shown as an inset on the left-most plot in Fig. 4-4 is not currently possible at MIT, yet is something which the simulation readily provides.

There is also great interest in the community in reaching photon energies above roughly 280 eV, within what is known as the x-ray “water window” where carbon has a high absorption coefficient. However, argon has a relatively low ionization energy, which means that ionization occurs too quickly and reaching these photon energies becomes impossible. However, by using a gas with a higher ionization energy, such as neon, one can increase the laser intensity and extend the HHG cutoff to generate energy within the water window. We recently conducted such an experiment and observed photons within the water window. Once again, the

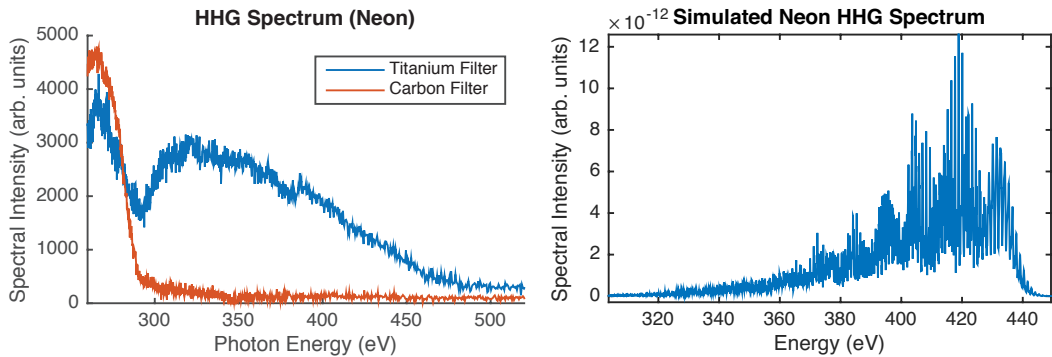


Figure 4-5: Experimental (left) and simulated (right) plots for water window high harmonic generation in neon gas. Though the spectra appear to differ, due to the certain post-high-harmonic-generation effects not considered in the simulations, the significant spectral features, including the high harmonic cutoff energy, are in relatively good agreement. Details regarding the discrepancies between the two can be found in the text.

simulation package can be used to make observations about the spectrum.

The experimental and simulation results can be found in Fig. 4-5. The experimental results, on the left, show the transmission through two different metallic filters, which are necessary to block the infrared driver pulse before measurement on the spectrometer. The lack of transmission through the carbon filter above roughly 280 eV is indicative of having entered the “water window” range. However, one may notice that there is also a dip in the spectrum for the titanium filter. This is caused by carbon contamination in the system, which is extremely difficult to avoid. The important spectral feature to consider is the high harmonic cutoff, which is in relatively good agreement between the experiment and the simulations. The simulation curve shown was generated with the same simulation code as above, but using 1.5 bar of neon and laser pulses with 1.35 mJ, 45 fs, and a focal spot of 40 μm .

Though the energy regions in which HHG is observed match rather well between the experimental and the simulated spectra, the shapes of the spectra are not particularly close. There are a number of reasons for this discrepancy. The

first was mentioned above: carbon contamination and the presence of the titanium filter. Fortunately, besides the spectral feature surrounding 280 eV in the titanium spectrum, this has little effect. What the simulation does not include is the response of the optics after the high harmonic generation (which precede the spectrometer) and the response of the spectrometer itself. In particular, there are multiple gold surfaces, one for the toroidal mirror and another for the diffraction grating. Each of these causes an energy-dependent reflection loss, such that higher energies have a lower reflectivity. Finally, the recombination amplitude used in the simulations is only approximate, and the more exact neon recombination amplitude (which is not immediately available at the time of this writing) drops off as energy increases, thereby increasing this spectral dependence. These effects combined, once included in the simulations, would lead to a much better agreement between the two plots. In addition, the absolute flux measurements from both the experiment and the simulations have yet to be rigorously calculated. All of these present excellent opportunities for future work.

Chapter 5

Pulse Compression in Kagome Fibers

The creation of ultrashort pulses is highly desirable for experiments done in the Kärtner group at MIT. As was introduced in Ch. 1, the nonlinear properties of a system may be exploited to generate additional frequency components that are then used for compression, as in Fig. 1-2. This can be used to create pulses which are shorter than the transform limited duration of the input, which is otherwise restricted by the uncertainty principle. The most straightforward form of nonlinear pulse compression involves propagation through a material, such as a gas, which has a predominantly third order nonlinear susceptibility $\chi^{(3)}$. As in Sec. 2.3.1, a third order susceptibility can give rise to self-phase modulation, which can cause spectral broadening through local, instantaneous changes in phase.

In the presence of diffraction, this effect can be short lived if peak powers are not sufficiently high. However, a confining geometry can be employed to extend the region of nonlinear interaction. This is used to enhance the spectral broadening, and allows for the creation of even shorter pulses. One such confining geometry is the Kagome Hollow-Core Photonic Crystal Fiber (HC-PCF),

which, because of its hollow core, can be used at extremely high peak powers. In addition, pulses propagating through the fundamental mode of the Kagome fiber experience extremely low losses[10]. This chapter studies the phenomenon of pulse compression in Kagome HC-PCF, which has demonstrated high-efficiency compression of energetic, ultrashort pulses.

The chapter is structured as follows. In Sec. 5.1, the theory of pulse compression is introduced and typical properties of the Kagome fiber are given in more detail. In particular, this section includes a discussion of the phenomenon of modulational instability, which will be important for the remainder of the chapter. Sec. 5.2 will show the experimental and simulated results for two different parameter regimes, inspired by recent experiments involving Kagome fiber pulse compression. Finally, in Sec. 5.3, the results of the experiments will be contrasted, and a path to a more effective Kagome HC-PCF pulse compressor will be discussed.

5.1 Compression and Modulational Instability

Following the analysis from Ch. 2, in the presence of self-phase modulation, a third order susceptibility, the propagation equation of interest for a non-diffracting pulse is

$$\frac{\partial E}{\partial z} = i\hat{n}_{\text{eff}}E - \frac{3i\chi^{(3)}\hat{\omega}}{8\hat{n}c}|E|^2E \quad (5.1)$$

where $E(\mathbf{x}, t, z)$ is the electric field and \hat{n}_{eff} is the effective refractive index. In addition, it is assumed that E is linearly polarized, which, while not true in general, will be satisfied for the remainder of the chapter. Notice also that the dispersion term, ∇_{\perp}^2 is not present, because the pulse can be written in terms of the modes of the fiber, which do not change during propagation. However, each mode will experience a *geometric phase*, the contribution of which is added through the

differential geometric refractive index $d\hat{n}_G$. With this term, the effective index can be written as

$$\hat{n}_{\text{eff}} = \hat{n} + d\hat{n}_G - n_g \quad (5.2)$$

where \hat{n} is the refractive index of the material and n_g is the group index¹.

Equation (5.1) describes the evolution of the 3D pulse as it propagates through the fiber. However, if the nonlinearity is relatively low, then the Kagome fiber displays a property known as *inhibited coupling*[10], in which energy in the fundamental mode, with a mode profile $M_1(\mathbf{x})$, cannot couple into higher order modes. Consequently, if all of the energy in the pulse is contained in the fundamental mode of the fiber at the input, it will stay in the fundamental mode during propagation. Making this approximation allows for a simplification of the propagation equation. Since the spatial profile of the pulse is known, the field $E(\mathbf{x}, t, z)$ can be decomposed into a spatial part and a component $E_1(t, z)$ which depends on t and z :

$$uE(\mathbf{x}, t, z) = E_1(t, z)M_1(\mathbf{x}) = E_1(t, z)|M_1(\mathbf{x})\rangle \quad (5.3)$$

where $|M_1(\mathbf{x})\rangle$ is the ‘ket’ associated with the fundamental (first) mode of the Kagome fiber².

In order to calculate the one-dimensional equation for fundamental mode propagation, one can plug Eq. (5.3) into the three-dimensional propagation equation Eq. (5.1) to obtain

$$\frac{\partial E_1}{\partial z}|M_1\rangle = i\hat{n}_{\text{eff}}E_1|M_1\rangle - \frac{3\chi^{(3)}\omega_0}{8n(\omega_0)c}|E_1|^2E_1||M_1|^2M_1\rangle \quad (5.4)$$

Taking the inner product (by applying $\langle M_1|$, the ‘bra’) with this equation yields

¹The group index is a free parameter which can be tuned for the simulation to ensure that the pulse does not leave the center of the moving frame.

²Here Dirac notation has been employed to represent the fundamental mode of the fiber, because it will allow us to more conveniently write inner products in later equations

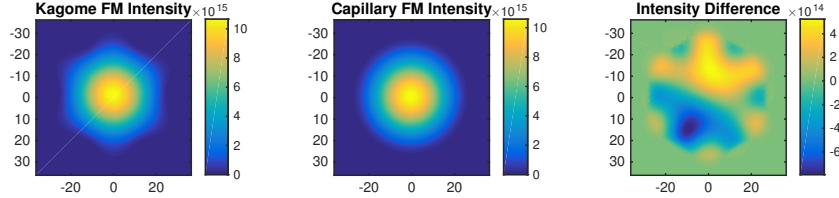


Figure 5-1: Plots of the fundamental mode (FM) profiles for a 7-cell Kagome fiber and a Cylindrical Capillary of comparable radii, corresponding to a capillary core radius of $29 \mu\text{m}$. Also shown is the difference between the two profiles, which shows good agreement between the two profiles. Because of the $\pi/3$ rotational symmetry in the Kagome fiber, the profile is roughly hexagonal, while the capillary and its profile are both rotationally invariant.

the one-dimensional propagation equation:

$$\frac{\partial E_1}{\partial z} = i\hat{n}_{\text{eff}}E_1 - g_{\text{SPM}} \frac{3\chi^{(3)}\omega_0}{8n(\omega_0)c} |E_1|^2 E_1 \quad (5.5)$$

where the nonlinear coupling coefficient g_{SPM} is given by

$$g_{\text{SPM}} = \frac{\langle M_1^2 | M_1^2 \rangle}{\langle M_1 | M_1 \rangle} = \frac{\int_{\mathbb{R}^2} d\mathbf{x} |M_1|^4}{\int_{\mathbb{R}^2} d\mathbf{x} |M_1|^2} \quad (5.6)$$

The value of this term is bounded by $[0, 1]$ and will lessen the strength of the nonlinear term.

For the 7-cell Kagome fiber geometry shown in Fig. 1-1, the intensity profile of the fundamental mode is given by the leftmost plot in Fig. 5-1. This is seen to match very closely the fundamental mode (FM) intensity profile of a hollow cylindrical capillary with a diameter $D = 58 \mu\text{m}$ [23]. The capillary mode is shown in the middle plot in Fig. 5-1. The difference between these two profiles is shown on the right, and reinforces the notion of their similarity. In fact, the coupling efficiency between the the two profiles is greater than 99.2%. Relatedly, for the

profiles shown in Fig. 5-1, the two SPM geometric factors are:

$$\begin{aligned} g_{\text{SPM,Kagome}} &= 0.5575 \\ g_{\text{SPM,Capillary}} &= 0.5656 \end{aligned} \quad (5.7)$$

compared to $g_{\text{SPM}} = 1$ for a plane wave. As we would expect, these factors are also very similar to one another. Finally, it should be noted that these factors hardly change as a function of their core radii (in part because they are both unitless), and can be considered constant properties of the respective geometries.

Because the mode profiles are so similar to one another, the dispersion profiles are also expectedly very similar. In fact, the dispersion of the Kagome fibers is often approximated to be identically the analytic formula for hollow cylindrical capillaries[33, 23] so that the geometric contribution to the refractive index is

$$n_{\text{eff}}(\omega) = \sqrt{n_{\text{gas}}^2(\omega) + \frac{u_{01}^2}{k^2(\omega)R^2}} \quad (5.8)$$

where $R = D/2$ is the effective radius. However, unlike the glass capillaries, the fundamental mode is well-confined, which means that the loss is almost negligibly low for the propagation distances of interest [19, 17, 10] and is ignored.

Because the properties of the Kagome fiber and the capillary are so similar, the analytic expressions for the capillary are used for the rest of this analysis. In addition, using the analytic expressions can help to avoid numerical artifacts and resonances often seen in finite-element calculations of the Kagome fiber properties. However, it also allows for simulations of experimental behavior for fibers for which finite-element-calculated data is not readily available. Ultimately, the differences between the geometries will be inconsequential for the parameter values of interest, and the distinction between the two will not be discussed again.

Under certain experimental conditions at high peak powers, it is well-known[1]

that fluctuations or noise on the input can experience gain during propagation, brought about by the nonlinearity. To see this, Eq. (5.5) can be seeded with a continuous wave beam, with frequency ω_0 , of constant field amplitude E_c . In this case, if the group index n_g is chosen such that the total refractive index vanishes at the frequency of interest, the solution is easily calculated to be

$$E_0(z, t) = E_c \exp \left[-iE_c^2 \frac{3g_{\text{SPM}}\chi^{(3)}\omega_0}{8n(\omega_0)c} z - i\omega_0 t \right] = E_c \exp [-i|E_c|^2 \gamma z - i\omega_0 t] \quad (5.9)$$

where γ is the nonlinear parameter, a convenience parameter. The z term in the exponential is a nonlinear phase which the pulse accumulates as a function of time.

This solution changes when noise (or any sort of modulation) $N(z, t)$ is added to the pulse. When

$$E_0 = (E_c + N) \exp [-i\gamma|E_c|^2 z - i\omega_0 t] \quad (5.10)$$

is tried as a solution, what remains of Eq. (5.5) can be linearized, to give an equation for the modulation[15]

$$\frac{\partial N}{\partial z} \approx i \frac{\beta_2}{2!} \frac{\partial^2 N}{\partial t^2} - \frac{\beta_3}{3!} \frac{\partial^3 N}{\partial t^3} - i \frac{\beta_4}{4!} \frac{\partial^4 N}{\partial t^4} - i\gamma|E_c|^2 (N + N^*) \quad (5.11)$$

where β_i is the i th term of the Taylor series of $\beta = \hat{n}_{\text{eff}}\hat{k}_0$ expanded about ω_0 , which is done so that the equation may be solved analytically. The β_1 is a free parameter, set by tuning the group refractive index n_g (which tunes the velocity of the reference frame), and is chosen to be zero. Similarly, β_0 does not control the dispersion relation and can be ignored. A trial solution of the form

$$N = N_+ \exp [ik(\Omega)z - i\Omega t] + N_- \exp [-ik(\Omega)z + i\Omega t] \quad (5.12)$$

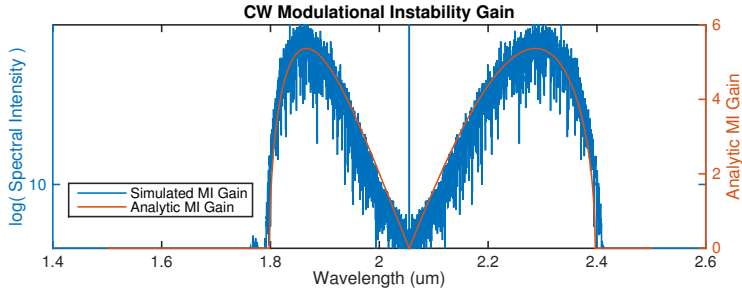


Figure 5-2: Plot comparing the simulated gain versus the analytic model. Note how well the two profiles agree with one another. At low noise levels, the additional terms ignored by the analytic model make very little difference, however, as is discussed later on, this approximation eventually falls apart.

may be used, where Ω is the frequency deviation from ω_0 . With such a wave-like solution, a dispersion relation should be derivable by plugging Eq. (5.12) into Eq. (5.11). This yields[15]

$$k(\Omega) = -\frac{\beta_3 \Omega^3}{3!} \pm \left[\left(\frac{\beta_4 \Omega^4}{4!} + \frac{\beta_2 \Omega^2}{2!} \right) \left(\frac{\beta_4 \Omega^4}{4!} + \frac{\beta_2 \Omega^2}{2!} + 2\gamma |E_c|^2 \right) \right]^{1/2} \quad (5.13)$$

From this equation, it can be seen that the value of the wavevector k can become complex under certain conditions. In particular, this can occur in the regime of anomalous dispersion, for which $\beta_2 < 0$. When the wavevector is complex, the modulation on the beam will experience exponential gain, and can eventually overwhelm the beam itself. Unfortunately, at relatively low gas filling pressure, just a few bar, the net dispersion in the Kagome fiber used in our group is anomalous over the entire bandwidth of the fiber, which extends from $1.5 \mu\text{m}$ to $2.5 \mu\text{m}$.

A comparison of a fully simulated model versus the analytic gain curve from Eq. (5.13), for a continuous wave beam passing through an $85 \mu\text{m}$ diameter Kagome fiber with 2 bar of Argon and at a peak power of 198 MW, is shown in Fig. 5-2. The simulated model is seeded with broadband white noise and allowed to propagate for roughly 1.5 meters. The agreement between the two profiles is

very good, and, in particular, the gain cutoffs around $1.8 \mu\text{m}$ and $2.4 \mu\text{m}$, match almost exactly, thus confirming that the simulation and theory match one another.

The modulational instability is a fundamentally continuous wave phenomenon; it describes the behavior of a continuous wave beam in the presence of a time-varying modulation. By contrast, clean pulse compression only occurs when the envelope is strongly time-varying, enough to prevent break up by modulational instability. The remainder of this section will discuss the propagation dynamics of a few different regimes of ultrashort pulses, in which the characteristic signatures of both effects can be observed. Ultimately, the onset of modulational instability can spell doom for a nonlinear pulse compressor, in which a clean temporal beam profile is desired at the output.

5.2 Pulse Compression Results

This section will delve into two different regimes for studying pulse compression in Kagome HC-PCF. The first of these is a slightly simplified case of a recent publication by Balciunas[4]. Here, an 80 fs pulse centered at $1.8 \mu\text{m}$ undergoes *self-compression*, where the ultrashort pulse is simultaneously broadened spectrally by the nonlinearity and linearly compressed by the anomalous dispersion of the system. The second situation, following a series of experiments in our group, involves propagation of an energetic 3.4 ps pulse centered at $2.06 \mu\text{m}$. It will be shown that this second scenario is far less stable, and, in the presence of a broadband noise modulation on the input, the pulse can devolve into a shower of individual spikes in intensity.

5.2.1 Mid-Infrared Self-Compression

In many experiments involving nonlinear pulse compression, the term ‘compressor’ is perhaps a misnomer; often the entire experimental setup consists of two parts[14]: one in which the self-phase modulation nonlinearity is exploited to introduce new spectral components, resulting in a positively chirped pulse, and another device (such as a grating pair) which can apply the linear dispersion necessary to compensate for the chirp. By contrast, self-compression, as was briefly introduced above, refers to the process by which the dispersion of a pulse is sufficiently large compared to the chirp created by the nonlinearity and of the right sign so that, during propagation, the pulse is both broadened and compressed. This process can yield a pulse which is nearly transform limited, and keeps most of the energy from the input in a single, compressed peak at the output.

This was the goal of a recent experiment conducted by Balciunas[4] in a recent publication featured in Nature Communications. In this paper, they propagated a $25 \mu\text{J}$, 80 fs pulse centered around $1.8 \mu\text{m}$ through a 20 cm segment of an $82 \mu\text{m}$ core-diameter Kagome fiber. In addition, the fiber is filled with 4 bar of Xenon gas, which acts as a nonlinear medium.

At the intensities reached during propagation, Xenon can experience some ionization, which will lead to plasma effects. In the publication, plasma effects and those introduced by the Higher Order Kerr Effect, often referred to as HOKE, are considered. Though these effects are necessary to more accurately reproduce experimental behaviors, they serve only to obfuscate the understanding of the behavior in most cases and, for this case in particular, they do not have a profound influence on the results. As such, these effects are not considered in detail here³, and Eq. (5.5), which includes only linear dispersion and self-phase modulation,

³The simulation package introduced here is certainly capable of including these effects, however, it is easier to discuss the results without being bogged down with a sea of ultimately insignificant nonlinear effects.

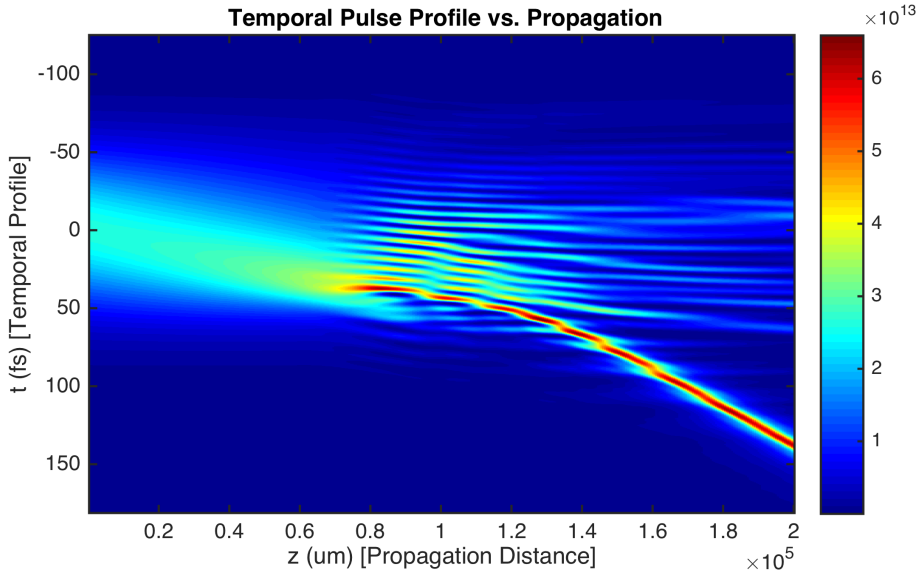


Figure 5-3: Simulations matching the parameters of Balciunas et al[4] showing the evolution of the temporal profile of the 80 fs pulse as it propagates through 20 cm of Xenon-filled Kagome fiber. During propagation, the pulse experiences self-compression, and produces a single soliton-like pulse at the output. The colorbar on the right displays the field intensity.

is solved using the parameters given above. In addition, the guidance bandwidth of the fundamental mode of the fiber is limited to $1.0 \mu\text{m}$ and $2.5 \mu\text{m}$ (as in the publication). This sort of limited bandwidth guidance is typical of photonic bandgap fibers such as the Kagome HC-PCF.

The results of running this simulation can be found in Fig. 5-3, which shows the temporal profile as a function of propagation distance through the Kagome HC-PCF, and Fig. 5-3, which shows some selected temporal profiles. Clearly, though the pulse begins with a Gaussian temporal profile, Fig. 5-4(a), after roughly 6 cm the pulse begins to compress. Self-steepening, the name given to the frequency dependent behavior of self-phase modulation, introduces a temporal asymmetry which quickly leads to the formation of a shock, Fig. 5-3(b). This process is expedited by a growing modulation on the pulse envelope, which forms because of the limited transmission bandwidth of the fiber mode.

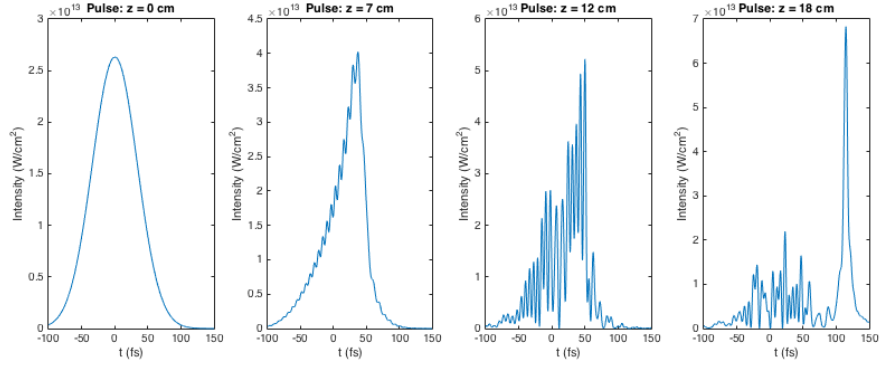


Figure 5-4: Individual temporal profiles corresponding to vertical cuts taken from Fig. 5-3. As the pulse propagates, a modulation forms and grows until, after the formation of an optical shock, a stable pulse forms at the output.

By the point at which the pulse has propagated 12 cm, Fig. 5-4(c), the pulse appears to have been completely pulled apart into separate intensity peaks, with a dominant periodicity corresponding to that of the envelope modulation, displaying behavior similar to that of modulational instability. However, it is clear in Fig. 5-4(d) that a single, strong, isolated pulse is generated. This single pulse behaves as a *soliton*, a self-stable solution in which the linear dispersion and the phase from self-phase modulation exactly cancel out one another[35]. As in the publication, somewhere around half of the energy is contained within the single peak. Here, however, the peak intensity of the pulse is 6×10^{13} W/cm², which is roughly double that of the result in the paper. This is because plasma effects are not considered, which would no doubt limit the strength of this peak.

By contrast to the results shown in the publication, Fig. 5-5 shows how the pulse evolves in the same pulse compression system if its input energy and duration is doubled, so as to keep the peak intensity fixed between the two cases. In this case, rather than self-compressing into a single pulse, two peaks form at the output, making the resulting profile less useful for experiments. This demonstrates that, despite the effectiveness of the compressor in the publication, self-

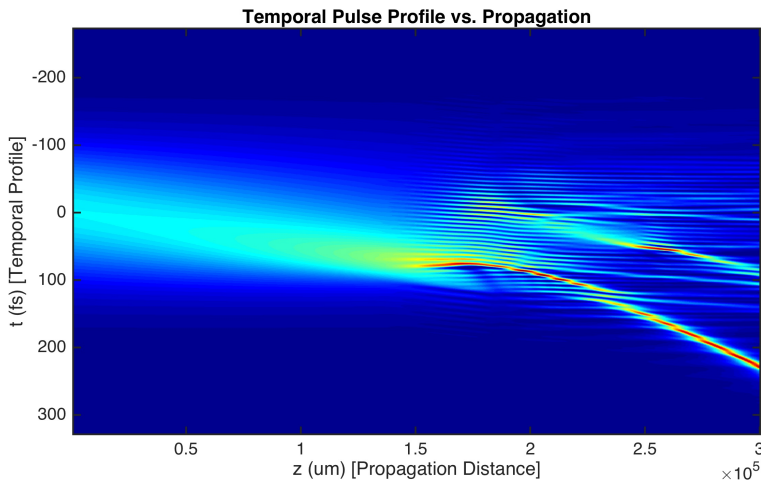


Figure 5-5: Evolution of a pulse as it passes through a Kagome fiber compressor as in Balciunas et al[4]. However, unlike the publication and the results shown in Fig. 5-3, the input pulse energy and duration are doubled (so as to keep the peak intensity fixed). This results in the formation of two peaks at the output, rather than a single soliton. This shows how the pulse compressor may be limited in the sorts of inputs it can handle.

compression may be limited in the types of pulses it can handle. This will be discussed in further detail in Sec. 5.3.

5.2.2 Picosecond Mid-Infrared Experiments

Kagome fibers have shown great promise for generating self-compressed pulses from sub-100 fs inputs, though their effectiveness for compressing picosecond pulses has yet to be explored. In our group, we had 3.4 ps, 2.06 μm seed pulses of energies up to 1.1 mJ at a 1 kHz repetition rate available. This setup relies on the amplification of 160 fs pulses generated by a holmium fiber oscillator using a Ho:YLF regenerative amplifier and an additional single pass amplifier. More details regarding the laser can be found in an upcoming publication. Ultimately, these 3.4 ps pulses cannot reach the sorts of peak intensities desired for studying extreme nonlinear phenomena, including high harmonic generation. As such,

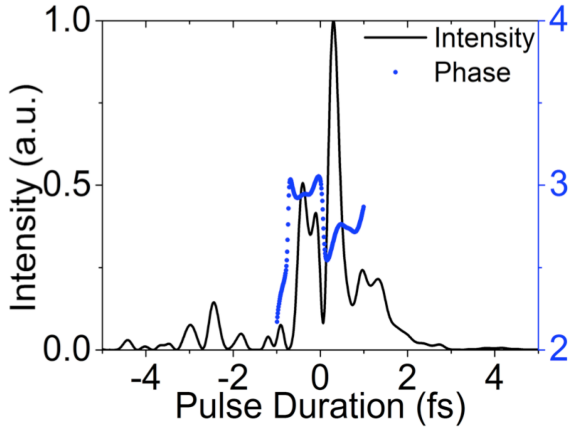


Figure 5-6: Experimental retrieval of the output field (from a FROG) of our Kagome fiber pulse compressor for a $560 \mu\text{J}$ input energy. There is a clear, sharp temporal feature which is mostly compressed which contains just under 40% of the pulse energy.

nonlinear pulse compression is necessary, and $2 \mu\text{m}$ guiding Kagome fiber was obtained from the group of Fetah Benabid for this purpose. Two different fibers are used in the experiments: one is a 7-cell geometry with a $57 \mu\text{m}$ effective core diameter and the other is a 19-cell fiber with an $85 \mu\text{m}$ core diameter. Though the dispersion is different between the two fibers, the largest difference between the different sets of experiments is the change in the peak intensity of the guided laser pulses, which can dramatically change the rate at which nonlinear effects occur. For most of the experimental results, and all of the simulations discussed here, a 4 m long section of fiber was used for propagation and pumped (on one side) with 3 bar of Argon gas. Finally, the coupling efficiency into the fibers is reliably above 90%, even at high input energies.

Experimental spectra of pulses propagated through this setup expectedly show spectral broadening. In addition, as the input pulse energy is swept from $61 \mu\text{J}$ to $500 \mu\text{J}$ while passing through the 7-cell ($57 \mu\text{m}$) Kagome fiber, the amount of spectral broadening increases, since the strength of the effect is dependent on the peak intensity of the pulse. The most interesting behavior, however, occurs

around $560 \mu\text{J}$ and is shown in Fig. 5-6. The results show that the output pulse has a relatively sharp peak in intensity, which contains roughly $190 \mu\text{J}$ (38%) of the input energy and has a full-width at half-maximum (FWHM) duration of 290 fs: an 11-fold decrease in duration. In addition, the peak is mostly transform-limited at the output. At energies beyond those at which this behavior is observed, damage begins to occur near the output of the fiber. In order to understand these behaviors, (1) the generation of multi-peaked structures and (2) the onset of damage, simulations became necessary.

The simulation package introduced in this thesis was adapted to match the experimental parameters used above. SHG-FROG measurements showed that the temporal profile of the input pulses was roughly Gaussian in nature, so the input pulses for the simulation are made to be Gaussian. As the pulse propagates, it undergoes spectral broadening and anomalous dispersion, as in the previous section. However, the spectrum of the 3.4 ps pulse is too narrow and, even after propagating for 4 m through the fiber, the pulse envelope does not change very much, despite the pulse undergoing a fair amount of nonlinear broadening. This can be seen in Figs. 5-7(a,d), which show the input and output intensity (a) and spectrum (d) profiles for this setup. Ultimately, the linear dispersion is far from enough (over this length-scale) to cancel out the positive chirp from the self-phase modulation, and this result fails to elucidate the more complex behavior observed in the experiments.

In truth, the pulses entering the setup are not perfectly Gaussian, and a modulation must be introduced in the simulation to make the pulse more realistic. In another few sets of simulations, different aperiodic modulation pedestals were added to the input and the behavior of the pulse was observed. As the pulse propagates through the fiber, the envelope modulation grows, just as in modulational instability. The addition of a weak spectral pedestal of FWHM bandwidth of

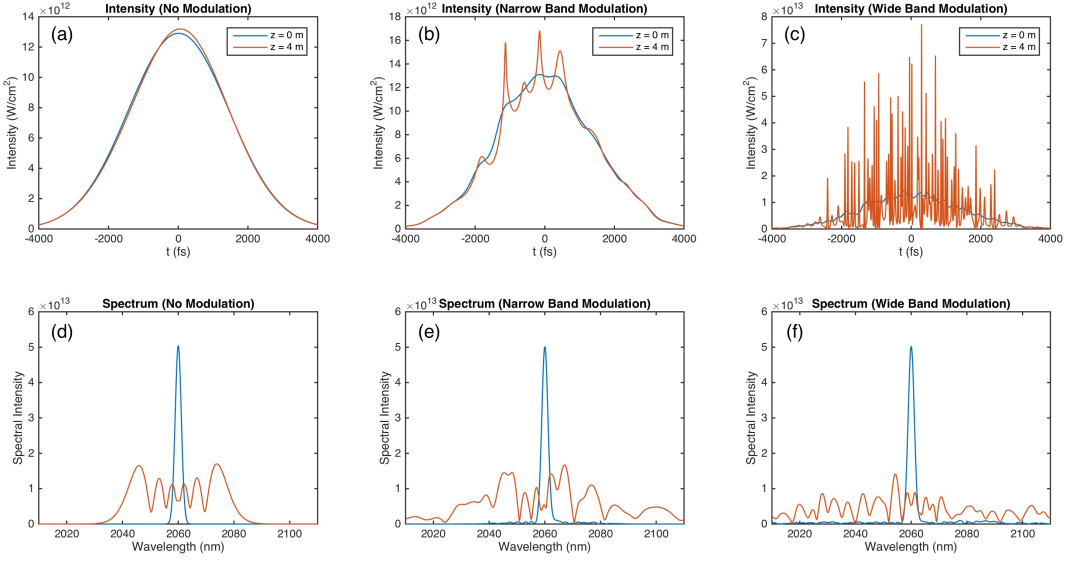


Figure 5-7: Simulated Kagome fiber compression results (temporal profiles and spectra) illustrating the effects of adding an aperiodic modulation to the pulse. Three different pulses are propagated through a 4 meter Kagome fiber: one without a pedestal, one with a narrow-band pedestal, and one with a wide-band pedestal. As the bandwidth of the pedestal is increased, the output profile is increasingly distorted, which can result in sharp intensity peaks.

$\Delta\omega = 5$ Thz, introduces ripples on the pulse envelope. The result of propagating a pulse with such a pedestal added is shown in Figs. 5-7 (b) and (e). Though the pedestal is barely visible in (e), it results in a clearly visible modulation on the pulse envelope. As the pulse propagates, the modulation ripples each experience some self-phase modulation and are each individually compressed. This leads to rather dramatic peaks in the intensity profile and, based on the structure of the input modulation, can create dramatic asymmetries at the output. In addition, as propagation continues, the peaks will continue to grow until they are compressed during propagation. The evolution of the intensity profile as a function of propagation is shown in Fig. 5-8, which illustrates how the peaks and troughs in the pulse envelope exaggerate and grow. These behaviors are reasonably consistent with the observed experimental results; a small pedestal can lead to the forma-

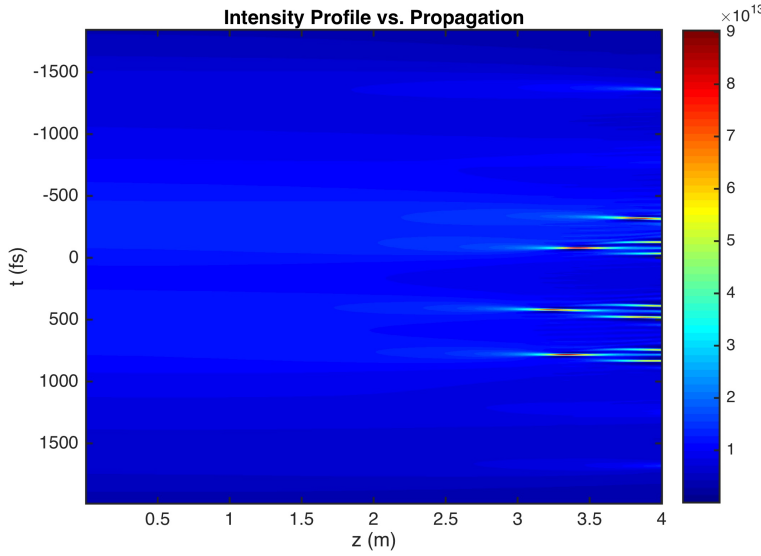


Figure 5-8: Intensity profile evolution as a function of propagation distance for a narrow-band modulation. Even though the bandwidth of the pedestal at the input is relatively narrow, the profile still splits into isolated peaks by the output. After the peaks form, they do not behave as solitons and continue to change in the presence of dispersion. The *forking* behavior, in which each peak splits into separate peaks after further propagation, is typical for an overly-dispersion-compensated pulse-compressor.

tion of partially or fully compressed peaks. In addition, the sharp intensity peaks could couple to spatial nonlinearities which would have the potential to damage the fiber if propagation continues for sufficient distances, as in the experiment.

As the bandwidth of the pedestal is increased, the effects of the modulational instability growth are even more dramatic, as one would expect from inspection of the analytic gain curve featured in Fig. 5-2. The temporal profiles and spectra for a wider-band (by a factor of 4) modulation are found in Figs. 5-7 (c) and (f). They show the dramatic effect that even a small pedestal has on the output profile, which is unrecognizable as having been Gaussian-like at the input. The train of pulses at the output is effectively useless for precision experiments in which accurate measurements of the envelope are necessary. In addition, the individual peaks continue to interfere with one another and evolve as propagation continues.

Finally, the strength of the pedestal is largely irrelevant; this behavior is very nearly always observed after sufficiently long propagation, which is indicative of modulational instability.

5.3 Pulse Compression Discussion

The difference between the results of Sec. 5.2.1 and Sec. 5.2.2 are striking. In the former, in which the input pulse is on the order of 10s of fs, self-compression of much of the input pulse energy is clearly possible, whereas in the latter, where the pulse duration hovers around a few ps, self-compression is largely impossible, limited by noise amplification. Two questions remain: under what conditions is the propagation limited by the modulational instability and what can be done to avoid the detrimental effects of modulation growth?

The efficacy of a Kagome fiber pulse compression system relies on a number of different parameters. From the linear and nonlinear terms in the differential equation, one can construct two *length* parameters, a linear length L_L and a nonlinear length L_{NL} , which are defined as follows[4]:

$$\begin{aligned} L_L &= \frac{|\beta_2|}{\tau_0^2} \\ L_{NL} &= \frac{1}{\gamma P_{\text{peak}}} \end{aligned} \tag{5.14}$$

where τ_0 is an appropriate time scale for the pulse, which is often assumed to be Gaussian, γ is the nonlinear parameter, and P_{peak} is the peak power of the pulse. These parameters can give a rough idea of the relative strengths of the linear and nonlinear phase terms in the differential equation. Since the dispersion of the Kagome fiber is quite low, especially in the presence of a high pressure gas, the nonlinear length is often dramatically shorter than the dispersion/linear length, unsurprisingly suggesting that the nonlinear coefficient is rather strong. Though

modulational instability has been studied for quite some time, this parameter space is relatively unexplored, in which the dispersion length can be orders of magnitude longer than the nonlinear length.

The relationship between these lengths is related to the formation of soliton pulses, which are self-stable solutions to the nonlinear propagation equation. It is important to note that solitons are relatively stable in the presence of a weak modulation as well. It is well established that a soliton will *shed* any energy that does not make up a part of the soliton profile. This occurs because a soliton, which readily accumulates nonlinear phase, experiences a slower effective group velocity, so that the soliton leaves behind the modulation during propagation. This prevents the growth of the modulation, as any particular region of the modulation is not above the threshold for growth for sufficiently long as to become a detriment. Soliton formation can be related to the *soliton order* parameter, N , which is a dimensionless parameter given by the square root of the ratio of the linear and nonlinear lengths[4]:

$$N = \sqrt{\frac{L_L}{L_{NL}}} = \sqrt{\frac{\tau^2 \gamma P_{\text{peak}}}{|\beta_2|}} \quad (5.15)$$

One may recognize that, for moderate soliton orders which hover just above unity, the pulse is in a regime in which the formation of a single peak is likely. However, for significantly higher soliton order values, the pulse is rather unstable, and can be substantially broken up by a modulation. For the main simulation in Sec. 5.2.1, N is roughly 11, which, as we would have expected, is within the regime within which we would expect that the pulse is capable of collapsing down to a single peak. By contrast, the experiments performed in our group, detailed in Sec. 5.2.2, have a soliton order which is over an order of magnitude higher, at just over 220. Clearly the picosecond pulse compression is ill-fated to be much more sensitive to a modulation on the input, a behavior which is reflected in the simulations.

A high soliton number places a limit on the promise of solitonic self-compression. The soliton number must be lowered, by changing the parameters in Eq. (5.15), for pulse compression to be effective. In particular, this can be done by lowering the gas pressure, which will lower the value of γ proportional to the pressure, and will slightly increase the magnitude of the dispersion. This strategy will then scale the distance which must be propagated to accumulate the same nonlinear phase, requiring a longer segment of Kagome fiber; however, doing this lowers the maximum compression factor which can be achieved by the compressor. A careful optimum must therefore be maintained: one in which the soliton order is reduced to the point of avoiding the multi-pulse breakup but also where N is not so low that the compression factor is still close to unity. The particular optimum will depend on the other parameters of the experiment.

Beyond the linear and nonlinear length scales, the specific details and limiting factors of the propagation depend on other parameters. First, the guidance bandwidth of the fiber can play a rather large role in determining the propagation dynamics. As was observed for the Balciunas result, when the spectrum grew to encounter the edge of the guidance band, a modulation was generated in the time domain. Were the input pulse not short enough to display soliton-like behavior, the modulation could have broken up the pulse into separate peaks. Finally, when the spectrum becomes sufficiently broad, the frequency dependence of the nonlinear response, often referred to as self-steepening, becomes more important. This can lead, in more extreme cases, to the formation of an optical shock, which can also destabilize the pulse.

The soliton number is determined almost exclusively by the properties of the input laser pulse, so many systems will not be within the regime in which solitonic self-compression is possible. However, it should be noted that, though self-compression may be stymied by modulational instability, two-stage pulse com-

pression is still readily achievable. Though still limited by the instability, cutting the fiber short before the modulation can grow to extreme magnitudes and compressing the pulse in a separate stage is an alternative route to pulse compression that, while characterized by lower compression factors, is a step in the desired direction.

Ultimately, however, the most promising path forward is to move to a region of positive dispersion. At a fundamental level, modulational instability is impossible, other than in specific, finely-tuned cases[15], in the positive dispersion regime. Working with positive dispersion comes at the expense of being able to achieve solitonic compression, as self-compression, like modulational instability, will only occur in negative dispersion, which is capable of canceling out the positive chirp introduced by the nonlinearity. Experimentally, this path is unclear, as relying on higher gas pressures to compensate for the naturally negative dispersion of the fiber often requires using 10s of atmospheres of pressure. In addition, having such a strong nonlinearity can introduce unwanted spatial effects. These complications may be avoided by moving to larger-core-diameter fibers, in which the dispersion is weaker and the peak intensities are more manageable.

In conclusion, solitonic self-compression is only stable within a specialized parameter regime, in which the soliton order is relatively low. Pulse compression of picosecond pulses in Kagome hollow core photonic crystal fibers is susceptible to the detrimental effects of modulational instability, which can reduce the overall effectiveness of the system in compressing the pulse. Finally, avoiding this complication involves moving to a regime of positive dispersion, though there are experimental complications in doing so.

Chapter 6

Conclusion & Future Work

In this thesis, I presented a simulation package for general ultrashort optical pulse propagation through nonlinear media written in MATLAB. The package takes a unique approach of modularity, which allows for simulation of more realistic experiments than more simple simulation codes otherwise allow. In addition, the architecture of the package allows for these setups to be constructed easily, with a minimal amount of configuration code on the behalf of the user. Finally, the classes in the code have been defined to ease the burden on the user in the way of plotting and additional data processing, which adds to the advantages of working within the package.

Even though the simulation code is easy to use, the framework I've introduced here also allows for a vast amount of customization, since the architecture itself was designed to be as general as possible. With this in mind, I emphasized that the framework is capable of supporting a variety of nonlinear optical effects, such that additional contributors can add nonlinear interactions between different fields of nearly any form. Wrapper functions have been provided so that wavemixing nonlinear effects, which are certainly the most popular class of nonlinearities, are extremely easy to translate to code from the coupled partial differential equations.

Furthermore, by subclassing the `npField` and `npCoord` nonlinear interactions between different sorts of fields can be made more efficient alongside the definition of custom nonlinear effects. To demonstrate this, I have shown a handful of use cases for the simulation code, ranging from analytically solvable linear and nonlinear results and a few more sophisticated use cases involving high harmonic generation.

Despite the enormous capabilities of the code, more work needs to be done to grow the base of the nonlinear effects. In particular, there are many different ways in which plasma can be generated and a multiplicity of theories to describe them. As of the time of this writing, only ADK ionization is supported. In addition, high harmonic generation can be calculated in a number of ways, so more robust HHG functionality should be included. This should be a motivating factor for future work.

The other focal point of this thesis was in applying the simulation package to studying the potential of nonlinear pulse compression in Kagome hollow core photonic crystal fibers. In particular, I explore the possibility of compressing picosecond pulses, which has otherwise not been achieved in Kagome fibers. In this vein, I investigate two different parameter regimes for pulse compression in these unique microstructured fibers. In the first regime, based upon a recent set of experiment conducted by Balciunas et al, looks at how 100 fs pulses at $1.8 \mu\text{m}$ can be efficiently self-compressed because of a confluence of favorable physical effects, including the finite guidance bandwidth of the fibers and relatively strong self-steepening. However, once the duration of the pulses is increased by a factor of two, these effects cannot overcome the detrimental effects of modulational instability, and self-compression to a single peak becomes impossible.

I also simulated recent experiments in our lab that studied the potential for Kagome fibers to compress pulses which were even longer in duration, up to

3 ps. Unfortunately, the propagation dynamics were mired by the growth of input modulation from modulational-instability. This effectively means that, like the result above, the pulses are simply too long to self-compress and avoid the detrimental effects of the modulation growth. This does not mean that two-stage compression cannot be done, and, in fact, this is how experimental efforts should proceed in the short term. In the long term, moving to positive dispersion could be particularly useful, since this undesired growth only occurs in the anomalous domain. Future work should study these effects more carefully, and investigate other parameter regimes in which the modulation instability may be avoided.

Bibliography

- [1] Govind P Agrawal. *Nonlinear Fiber Optics*. Academic Press, fourth edition, 2007.
- [2] M V Ammosov, N B Delone, and V P Krainov. Tunnel ionization of complex atoms and of atomic ions in an alternating electromagnetic field. *JETP*, 64(6):1191, December 1986.
- [3] J Armstrong, N Bloembergen, J Ducuing, and P Pershan. Interactions between Light Waves in a Nonlinear Dielectric. *Physical Review*, 127(6):1918–1939, September 1962.
- [4] T Balciunas, C Fourcade-Dutin, G Fan, T Witting, A A Voronin, A M Zheltikov, F Gérôme, G G Paulus, A Baltuska, and F Benabid. A strong-field driver in the single-cycle regime based on self-compression in a kagome fibre. *Nature Communications*, 6:1–7, January 2015.
- [5] Robert W Boyd. *Nonlinear Optics*. Academic Press, third edition, 2008.
- [6] Chun-Lin Chang, Peter R Krogen, Houkun Liang, Gregory J Stein, Jeffrey Moses, Chien-Jen Lai, Jonathas P Siqueira, Luis E Zapata, Franz X Kärtner, and Kyung-Han Hong. Multi-mJ, kHz, ps deep-ultraviolet source. *Optics Letters*, 40(4):665–4, 2015.
- [7] P B Corkum, P Balcou, Misha Yu Ivanov, Anne L’Huillier, and Maciej Lewenstein. Theory of high-harmonic generation by low-frequency laser fields. *Physical Review A*, 49(3):2117–2132, March 1994.
- [8] A Couairon and A Mysyrowicz. Femtosecond filamentation in transparent media. *Physics Reports*, 441:47–189, February 2007.
- [9] Sandro De Silvestri, Mauro Nisoli, Giuseppe Sansone, Salvatore Stagira, and Orazio Svelto. Few-Cycle Laser Pulse Generation and Its Applications. In Franz X Kärtner, editor, *Few-Cycle Pulses by External Compression*, pages 137–178. Springer-Verlag, 2004.

- [10] B Debord, M Alharbi, T Bradley, C Fourcade-Dutin, Y Y Wang, L Vincetti, F Gérôme, and F Benabid. Hypocycloid-shaped hollow-core photonic crystal fiber Part I: Arc curvature effect on confinement loss. *Optics Express*, 21(23):28597–28608, 2013.
- [11] F DeMartini, C H Townes, T K Gustafson, and P L Kelley. Self-steepening of light pulses. *Physical Review*, 164(2):312–323, 1967.
- [12] Daniele Faccio, Alexander Grün, Philip K Bates, Olivier Chalus, and Jens Biegert. Optical amplification in the near-infrared in gas-filled hollow-core fibers. *Optics Letters*, 34(19):2918–2920, October 2009.
- [13] M Geissler, G Tempea, A Scrinzi, M Schnürer, Ferenc Krausz, and T Brabec. Light Propagation in Field-Ionizing Media: Extreme Nonlinear Optics. *Physical Review Letters*, 83(15):2930–2933, October 1999.
- [14] J M Halbout and D Grischkowsky. 12-fs ultrashort optical pulse compression at a high repetition rate. *Applied Physics Letters*, 45(12):1281, 1984.
- [15] John D Harvey, Rainer Leonhardt, Stéphane Coen, Gordon K L Wong, JonathanC Knight, William J Wadsworth, and Philip St J Russell. Scalar modulation instability in the normal dispersion regime by use of a photonic crystal fiber. *Optics Letters*, 28(22):2225–3, 2003.
- [16] O H Heckl, C R E Baer, C Kränkel, S V Marchese, F Schapper, M Holler, T Südmeyer, J S Robinson, J W G Tisch, F County, P Light, F Benabid, and U Keller. High harmonic generation in a gas-filled hollow-core photonic crystal fiber. *Applied Physics B*, 97(2):369–373, October 2009.
- [17] O H Heckl, C J Saraceno, C R E Baer, T Südmeyer, Y Y Wang, Y Cheng, F Benabid, and U Keller. Temporal pulse compression in a xenon-filled Kagome-type hollow-core photonic crystal fiber at high average power. *Optics Express*, 19(20):19142–8, 2011.
- [18] Kyung-Han Hong, Chien-Jen Lai, Jonathas P Siqueira, Peter R Krogen, Jeffrey Moses, Chun-Lin Chang, Gregory J Stein, Luis E Zapata, and Franz X Kärtner. Multi-mJ, kHz, 2.1 μm optical parametric chirped-pulse amplifier and high-flux soft x-ray high-harmonic generation. *Optics Letters*, 39(11):3145–3148, May 2014.
- [19] Song-Jin Im, Anton Husakou, and Joachim Herrmann. Guiding properties and dispersion control of kagome lattice hollow-core photonic crystal fibers. *Optics Express*, 17(15):13050–9, 2009.

- [20] John D Jackson. *Classical Electrodynamics*. Wiley, third edition, 1998.
- [21] Anh-Thu Le, R Lucchese, S Tonzani, T Morishita, and C D Lin. Quantitative rescattering theory for high-order harmonic generation from molecules. *Physical Review A*, 80(1):013401, July 2009.
- [22] Houkun Liang, Peter R Krogen, Ross Grynko, Ondrej Novak, Chun-Lin Chang, Gregory J Stein, Darshana L Weerawarne, Bonggu Shim, Franz X Kärtner, and Kyung-Han Hong. Three-octave-spanning supercontinuum generation and sub-two-cycle self-compression of mid-infrared filaments in dielectrics. *Optics Letters*, 40(6):1069–1072, March 2015.
- [23] E A J Marcatili and R A Schmeltzer. Hollow Metallic and Dielectric Waveguides for Long Distance Optical Transmission and Lasers. *Bell System Technical Journal*, 43(4):1783–1809, July 1964.
- [24] MATLAB. *Version 8.4.0 (R2014b)*. The MathWorks Inc., Natick, Massachusetts, 2010.
- [25] Jeffrey Moses and Frank Wise. Controllable Self-Steepeening of Ultrashort Pulses in Quadratic Nonlinear Media. *Physical Review Letters*, 97(7):073903, August 2006.
- [26] Johannes Nold, P Hölzer, N Y Joly, G K L Wong, A Nazarkin, A Podlipensky, M Scharrer, and Philip St J Russell. Pressure-controlled phase matching to third harmonic in Ar-filled hollow-core photonic crystal fiber. *Optics Letters*, 35(17):2922–3, September 2010.
- [27] William H Press, Saul A Teukolsky, William T Vetterling, and Brian P Flannery. *Numerical Recipes: The Art of Scientific Computing*. Cambridge University Press, third edition, 2007.
- [28] Jinendra K Ranka and Alexander L Gaeta. Breakdown of the slowly varying envelope approximation in the self-focusing of ultrashort pulses. *Optics Letters*, 23(7):534–536, April 1998.
- [29] H Ren, A Nazarkin, Johannes Nold, and Philip St J Russell. Quasi-phase-matched high harmonic generation in hollow core photonic crystal fibers. *Optics Express*, 16(21):17052–8, 2008.
- [30] A E Siegman. Quasi fast Hankel transform. *Optics Letters*, 1(1):13–15, July 1977.

- [31] S Skupin and L Bergé. Self-guiding of femtosecond light pulses in condensed media: Plasma generation versus chromatic dispersion. *Physica D: Nonlinear Phenomena*, 220(1):14–30, August 2006.
- [32] Francesco Tani, John C Travers, and Philip St J Russell. Multimode ultrafast nonlinear optics in optical waveguides: numerical modeling and experiments in kagomé photonic-crystal fiber. *Journal of the Optical Society of America B*, 31(2):311–320, 2014.
- [33] John C Travers, Wonkeun Chang, Johannes Nold, Nicholas Y Joly, and Philip St J Russell. Ultrafast nonlinear optics in gas-filled hollow-core photonic crystal fibers. *Journal of the Optical Society of America B*, 28(12):A11–A26, November 2011.
- [34] Li Yu, Meichun Huang, Mouzhi Chen, Wenzhong Chen, Wenda Huang, and Zhizhong Zhu. Quasi-discrete Hankel transform. *Optics Letters*, 23(6):409–411, March 1998.
- [35] V E Zakharov and A B Shabat. Interaction between solitons in a stable medium. *Journal of Experimental and Theoretical Physics*, 64:1627–1639, May 1973.